

CO/H₂, C/CO, OH/CO, and OH/O₂ in Dense Interstellar Gas: From High Ionization to Low Metallicity

Shmuel Bialy^{*1} and Amiel Sternberg¹

¹Raymond and Beverly Sackler School of Physics & Astronomy, Tel Aviv University, Ramat Aviv 69978, Israel

^{*} shmuelbi@mail.tau.ac.il

Accepted: 2015 April 15. Received: 2015 March 30; in original form: 2014 September 23

ABSTRACT

We present numerical computations and analytic scaling relations for interstellar ion-molecule gas phase chemistry down to very low metallicities ($10^{-3} \times$ solar), and/or up to high driving ionization rates. Relevant environments include the cool interstellar medium (ISM) in low-metallicity dwarf galaxies, early enriched clouds at the reionization and Pop-II star formation era, and in dense cold gas exposed to intense X-ray or cosmic-ray sources. We focus on the behavior for H₂, CO, CH, OH, H₂O and O₂, at gas temperatures ~ 100 K, characteristic of a cooled ISM at low metallicities. We consider shielded or partially shielded one-zone gas parcels, and solve the gas phase chemical rate equations for the steady-state “metal-molecule” abundances for a wide range of ionization parameters, ζ/n , and metallicities, Z' . We find that the OH abundances are always maximal near the H-to-H₂ conversion points, and that large OH abundances persist at very low metallicities even when the hydrogen is predominantly atomic. We study the OH/O₂, C/CO and OH/CO abundance ratios, from large to small, as functions of ζ/n and Z' . Much of the cold dense ISM for the Pop-II generation may have been OH-dominated and atomic rather than CO-dominated and molecular.

Key words: ISM: molecules – galaxies: abundances – reionization, first stars – cosmic rays – X-rays: ISM

1 INTRODUCTION

In this paper we present a numerical and analytic study of interstellar gas-phase ion-molecule chemistry, from Galactic conditions into the relatively unexplored domain of interstellar media at very low metallicities, and related chemical properties at high ionization rates. Relevant astrophysical environments include the cool ISM in low metallicity dwarf galaxies, early enriched clouds at reionization and the Pop-II star formation epoch, and in dense cold gas exposed to intense X-ray or cosmic-ray sources. We consider the behavior for a wide range of initiating hydrogen ionization rates and gas densities. Our focus is mainly on the molecular cold-cloud chemistry for H₂, CO, CH, OH, H₂O and O₂, and the relative steady-state abundances of these species, for varying metallicities and ionization parameters. Our discussion includes a detailed analysis of the hydrogen-carbon-oxygen gas-phase chemical networks for cold gas in the transition to the low-metallicity limit.

There are several motivations for this work. First, observations of Population-II stars in the Galactic halo (Beers & Christlieb 2005) have revealed stars with heavy element abundances orders of magnitude smaller than in the Sun and the interstellar medium (ISM) of the star-forming disk. In the primitive halo star SDSS J102915+192927, for example, an overall metallicity of less than $10^{-4} \times$ solar has been reported (Caffau et al. 2011). In many metal-poor stars the carbon/iron ratios are significantly enhanced (e.g., Norris et al. 2013; Yong et al. 2013; Carollo et al. 2014) but even so the absolute carbon and oxygen abundances are very low, down to 10^{-3} compared to solar photospheric values. The very existence of these stars is evidence for interstellar media with metallicities far lower than in present-day galaxies. Here we ask, and considering gas-phase ion-molecule formation-destruction chem-

istry in a cold dense ISM how do the atomic and molecular constituents for the heavy elements, especially carbon and oxygen, depend on the overall metallicity, from solar down to very subsolar?

Star formation, and the processes that led to the metal poor Pop-II stars, probably included molecule formation to a level that enhanced gas cooling and regulated the Jeans masses. In pristine or in very low metallicity environments, even partial conversion to H₂ enables efficient rotational line cooling in addition to atomic and ionic metal fine-structure emissions (Bromm & Loeb 2003; Santoro & Shull 2006; Glover & Jappsen 2007; Omukai et al. 2010; Glover & Clark 2014). At high metallicities such as in Milky Way star-forming regions, complete conversion to H₂ occurs (e.g., Sternberg et al. 2014) enabling the associated production of heavy molecules (Graedel et al. 1982; van Dishoeck 1998; Tielens 2013). For the cold “dense-gas” components of the ISM, what are the most abundant molecules containing heavy elements? For normal Galactic conditions at solar metallicity this is CO, especially in regions shielded from photodissociating radiation. Is this true also for a metallicity of 10^{-3} ?

Very low metallicity stars have also been detected in nearby dwarf-spheroidal (dSph) galaxies (Tafelmeyer et al. 2010), e.g., most recently in the Galaxy satellite Segue 1 (Frebel et al. 2014). These dwarf galaxies may be directly related to the low-metallicity damped Ly α absorbers (DLAs) observed from low to high redshifts (e.g., Pettini et al. 2008; Penprase et al. 2010; Rafelski et al. 2012). The low DLA metallicities, e.g. down to $\sim 2 \times 10^{-3}$ in the ($z=5.1$) absorber toward the QSO J1202+3235 (Rafelski et al. 2012), and the similar elemental abundance patterns, suggest that the DLAs may represent the initial conditions for the low-metallicity Pop-II stars and dSphs. The relative abundance patterns, including α -element enhancements, appear consistent with nucleosynthetic pro-

duction in massive (initially metal-free) Population-III stars at the reionization epoch. Then, if ultra-low metallicity molecular clouds existed at reionization and in the protogalaxies in which the Pop-II stars formed, what were their chemical properties?

Atomic and molecular carbon/oxygen chemical networks have been included in models for the cooling and fragmentation properties of gravitationally contracting clumps and protostar formation at very low-metallicities (e.g., Omukai 2000; Schneider et al. 2002; Omukai et al. 2005; Schneider et al. 2006; Jappsen et al. 2009a,b; Dopcke et al. 2011; Klessen et al. 2012; Omukai 2012; Chiaki et al. 2013). In these models the chemistry is intrinsically time-dependent as molecules form via gas-phase sequences in collapsing clouds. The behavior is thus similar to molecule reformation zones behind dissociative shock waves (e.g., Hollenbach & McKee 1989; Neufeld & Dalgarno 1989). In contrast, the focus of our paper is on the chemical properties down to low metallicities of *ionization-driven systems*, for which well defined steady-states exist. This may be more appropriate for the chemical behavior of the bulk cold interstellar medium. Such ISM components may be virialized and not immediately collapsing, or not even gravitationally bound. As for the ISM in present-day galaxies we assume a (quasi) heating-cooling equilibrium. Thus our study is complementary to time-dependent models of the kind presented by Omukai et al. (2005) for which a steady-state is not defined.

A second motivation is the large range in ionization rates that may be expected for the neutral atomic/molecular ISM in galaxies from low to high redshift and with varying star-formation rate. For the standard neutral Galactic ISM, the ion-molecule chemistry and the production of “heavy molecules” is driven by (low-energy) cosmic ray ionization. The ionization rate, as probed by observations of H_3^+ , HCO^+ , OH , OH^+ , or H_2O^+ , in diffuse and dense gas, and in the intercloud medium (e.g., van Dishoeck & Black 1986; van der Tak & van Dishoeck 2000; Neufeld et al. 2010; Indriolo & McCall 2012) may vary with location in the Galaxy and with individual cloud thickness, but overall it seems to lie within the fairly narrow range $\sim 10^{-16}$ to 10^{-15} s^{-1} (Dalgarno 2006; Indriolo & McCall 2012). In as much as cosmic ray production depends on star-formation and the subsequent supernova explosions and shock particle accelerations, the internal ionization rates may be significantly larger in more rapidly star-forming and/or compact galaxies, compared to $3 \text{ M}_\odot \text{ yr}^{-1}$ within $\sim 10 \text{ kpc}$ for the Milky Way. At high redshift and along the upper end of the main-sequence for star-forming galaxies (Whitaker et al. 2012), or for merging star-bursting systems, the surface star-formation rates may be orders of magnitude larger than for the Galaxy (e.g., Förster Schreiber et al. 2009; Tacconi et al. 2013), and this may imply correspondingly very high cosmic-ray fluxes (Papadopoulos 2010; Bayet et al. 2011; Mashian et al. 2013). The galaxy mass-metallicity relation (Tremonti et al. 2004; Mannucci et al. 2010) may then also imply a correlation between metallicity and global ionization rate for the neutral ISM in galaxies.

The ionization rates may also be much larger than the characteristic Galactic value in localized environments exposed to X-rays, or enhanced cosmic-ray fluxes. Penetrating X-rays and cosmic-rays are largely equivalent in their chemical effects, since the hydrogen ionization is always due to the secondary electrons produced by either primary X-ray photoionization or cosmic-ray impact ionization (Lepp & Dalgarno 1996; Maloney et al. 1996; Meijerink & Spaans 2005). X-ray irradiation may play a dominating role in the inner envelopes and disks around young stellar objects (Igea & Glassgold

1999; Stäuber et al. 2005; Vasyunin et al. 2008). External to the Galaxy, X-ray driven chemistry may be especially important for any molecular gas around accreting massive black holes, from active galaxies in the local Universe (e.g., Hailey-Dunsheath et al. 2012) to high-redshift minihalos around the time of cosmic reionization (Volonteri & Silk 2014; Chen et al. 2014).

In this paper we consider “one-zone” models for the basic hydrogen, carbon, and oxygen gas-phase formation-destruction chemistry for idealized representative gas parcels, and we study the behavior as a function of the overall metallicity, Z' , of the gas. We assume that the gas temperatures are fixed by a radiative heating and cooling balance, but we do not explicitly solve for the gas temperature. As most recently indicated by Glover & Clark (2014), for radiative heating and cooling at low metallicity a major fraction of the gas mass may rapidly cool to temperatures of order 100 K via H_2 emission line cooling (see also Bovino et al. (2014) and Safranek-Shrader et al. (2014)). In our study we adopt 100 K as our fiducial cold gas temperature. We wish to understand how the molecular production efficiencies and pathways for the most abundant oxygen and carbon bearing species vary as the metallicity becomes very small, within the regime of (temperature-insensitive) cold-cloud chemistry. Thus, the essential parameters are the metallicity Z' (relative to solar) and the ratio of the driving ionization rate, ζ , to the gas density, n . We also consider the effects of partially attenuated background far-ultraviolet (FUV) radiation when or if dust shielding becomes ineffective, but we do not include any radiative transfer for the FUV.

We presented preliminary results for some of the computations presented in this paper in Sternberg et al. (2011). There have also been other analyses of heavy element molecular chemistry in the early Universe and at low-metallicity (see Yan 1997; Harwit & Spaans 2003; Dalgarno 2006; Vonlanthen et al. 2009; Pentado et al. 2014). Discussions of gas phase chemistry at very high ionization rates have also been presented (Lepp & Dalgarno 1996; Lepp & Tiné 1998; Bayet et al. 2011) but these have been restricted to local Universe environments, for solar or near-solar metallicities. In this paper we consider the low-temperature behavior for a very wide range of metallicities and ionization parameters.

In §2 we present our chemical networks and describe the dominant formation-destruction reactions and pathways. We also present a discussion of photoprocesses for partially shielded gas parcels. In §3 we write down and discuss the chemical rate equations, and define our adjustable parameters, Z' , ζ/n , and I_{UV}/n . In §4 we present an analytic treatment for the atomic to molecular hydrogen balance, and for the steady-state H_2 formation time scales. In §5 we develop our analytic scaling relations using 1D numerical model sequences for the chemical behavior as a function of metallicity at fixed ionization parameter, and vice versa. Our focus is on H_2 , CO , CH , OH , H_2O , and O_2 , and we discuss how the molecular abundance ratios vary with the parameters. In §6 we present comprehensive full 2D computations for the chemical behavior, spanning the range from low metallicity to high ionization parameter. In §7 we compare our results for ionization-driven chemistry in equilibrium gas to the time-dependent behavior for low-metallicity collapsing clouds. We summarize our results and discuss observational implications in §8.

2 CHEMICAL NETWORKS

We consider simplified (“minimal”) interstellar gas phase networks (Figures 1, 2, and 3) for the formation and destruc-

tion of H and H₂, and for the metal-bearing molecules, OH, H₂O, O₂, CH, and CO, which are our primary focus. The networks consist of standard ionization-driven two-body ion-molecule sequences, including selective neutral-neutral atom-exchange reactions, and moderated by dissociative and radiative recombination (Herbst & Klemperer 1973; Dalgarno & Black 1976; van Dishoeck 1988; Sternberg & Dalgarno 1995; van Dishoeck 1998; Le Teuff et al. 2000; McElroy et al. 2013; Wakelam et al. 2012). We assume that the ionization of H, H₂, and He is provided by a flux of penetrating cosmic-rays and/or X-rays, with a total (primary plus secondary) H₂ ionization frequency ζ (s⁻¹). We also consider destructive photoprocesses due to background FUV radiation.

At high metallicities, molecule formation on dust grains are important for the synthesis of heavy molecules and their introduction into the gas phase, especially H₂O and O₂. (e.g., Cuppen et al. 2010; van Dishoeck et al. 2013; Lamberts et al. 2014). Furthermore, temperature-dependent freezeout removes molecules from the gas phase, and alters molecular abundance ratios. These effects are also sensitive to optical-depth dependent radiation fields, as discussed for example by Hollenbach et al. (2009) and Hollenbach et al. (2012). However, with decreasing metallicity and dust-to-gas mass ratios, the relative importance of dust-grain formation of the heavy molecules is expected to diminish significantly compared to pure gas phase processes. Furthermore, the intrinsic dust properties are uncertain at low metallicities, and modeling these requires the introduction of additional free parameters. In this study we therefore focus on the well-defined metallicity dependence of just the gas-phase formation-destruction pathways. Thus, our models are idealized and we caution that for many realistic environments at high-metallicity our computed abundances could be modified by the inclusion of dust interactions.

Negative-ion chemistry (Dalgarno & McCray 1973; Walsh et al. 2009) plays a role only for H₂, via the H⁻ formation route, as described below. Negative ion production reactions for the heavy molecules are included in our set¹ but they remain negligible throughout. Our focus is on low-temperature $T \lesssim 300$ K gas for which the formation sequences are unaffected by direct H₂ neutral-neutral reactions² with large endothermicities or activation barriers. Our networks include a total of 74 atomic and molecular hydrogen, carbon, oxygen, nitrogen, silicon, and sulfur species, and a set of 986 reactions, of which around 80 play a significant role as we describe below.

We wish to study the basic variation trends of the steady-state abundances of the chemical species within isothermal and uniform density “gas parcels”, as functions of the gas phase elemental abundances or metallicity of the gas, the ionization rate, and the total hydrogen gas density. We are particularly interested in the behavior at very subsolar metallicities, and/or high ionization rates. We parameterize the metallicity by a scaling factor Z' , such that $Z' = 1$ corresponds to the heavy element abundances in the solar photosphere (Asplund et al. 2009) as listed in Table 1. We consider the solutions to the formation-destruction equations with and without the presence of a moderating and partially attenuated background FUV radiation field. Lyman continuum radiation is always excluded. When a background FUV field is present we assume that for sufficiently high metallicities the gas parcels are fully shielded by surrounding optically thick columns of dust. As Z' becomes

Table 1. Heavy element abundances relative to hydrogen.

Element	n_i/n
C	2.9×10^{-4}
N	6.8×10^{-4}
O	4.9×10^{-4}
Si	3.2×10^{-5}
S	1.3×10^{-5}

small we allow the gas to become optically thin to dust-absorption. However, we assume that the parcels are always shielded by sufficiently large columns of H₂ such that the 912-1108 Å Lyman-Werner (LW) band is fully blocked by fully overlapping H₂ absorption lines. We introduce this assumption to allow for optimal conditions for molecule formation in the parcels even at very low metallicity.

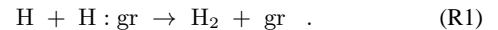
In our description of the networks we describe the dominant formation and destruction pathways in the limits of high and low metallicity. As we discuss in §4 and §5, for any Z' the hydrogen makes the transition from predominantly atomic to molecular form at a critical ratio of the ionization rate ζ to the total hydrogen gas density n . In our discussion, the high-metallicity formation-destruction pathways usually (but not always) correspond to predominantly H₂ gas. The low-metallicity pathways usually correspond to predominantly H gas. The transition from the fully H₂ “molecular regime” to the fully H “atomic regime” is important for the chemical behavior, as we describe below.

We begin with a description of the hydrogen/helium networks, and then consider the oxygen, and carbon/oxygen sequences.

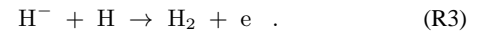
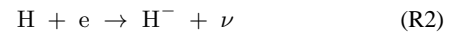
2.1 Hydrogen and Helium

We illustrate the hydrogen-helium networks in Figure 1. These networks include the species H, H₂, H⁺, H⁻, H₂⁺, H₃⁺, He, He⁺, and HeH⁺.

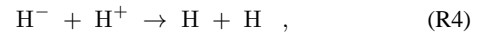
The formation of H₂ is essential for the efficient ion-molecule production of metal-bearing molecular species in the gas phase. At high metallicity H₂ formation is dominated by dust-grain catalysis



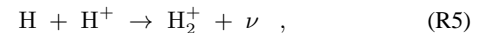
At sufficiently low metallicity the main H₂ formation route is in the gas phase via the formation of H⁻ negative ions



This radiative-attachment associative-detachment sequence is moderated by mutual neutralization



which limits the H⁻ abundances when the proton density becomes large. Gas phase H₂ production also proceeds via radiative association



followed by charge transfer



However, at the low gas temperatures ($T \lesssim 300$ K) we are considering, and in the absence of photodetachment, the H⁻ sequence, [R2] and [R3], always dominates.

¹ e.g., $\text{H}^- + \text{O} \rightarrow \text{OH} + \text{e}$

² e.g., $\text{O} + \text{H}_2 \rightarrow \text{OH} + \text{H}$; $\text{OH} + \text{H}_2 \rightarrow \text{H}_2\text{O} + \text{H}$

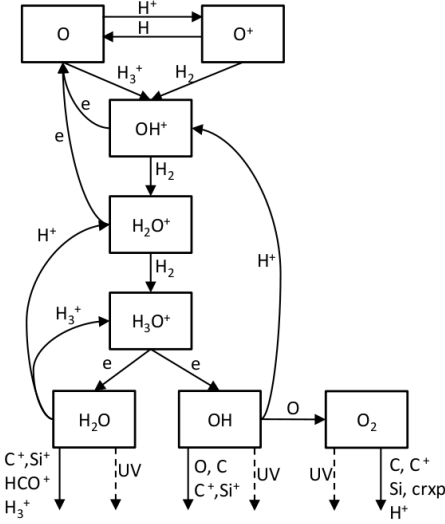
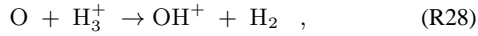
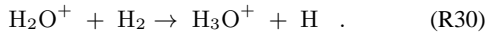
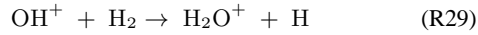


Figure 2. Ion-molecule formation-destruction pathways for OH, H₂O and O₂.

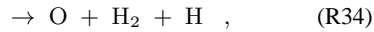
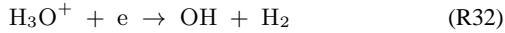
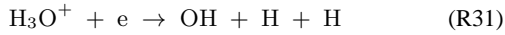
or by proton transfer



followed by the rapid abstractions



The sequence is terminated by dissociative recombination



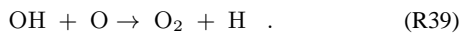
which yields the OH and H₂O molecules. When the fractional ionization is large, the abstraction sequence may be interrupted by dissociative recombination of the reactive ions



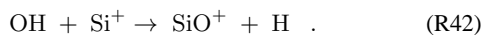
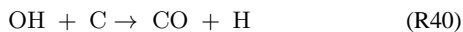
and



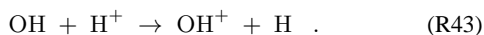
Importantly, at high metallicities OH is removed mainly by rapid reactions with oxygen atoms



Additional removal reactions are

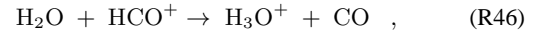
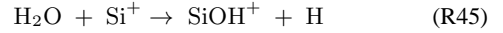
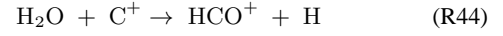


At low metallicity, OH is removed mainly by charge transfer with protons

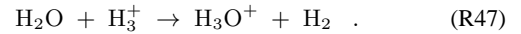


Reaction [R43] is a destruction channel because some of the OH⁺, H₂O⁺, and H₃O⁺ ions undergo dissociative-recombination leading directly to atomic oxygen and to the complete breakup of the chemical bonds. The transition from OH removal by oxygen atoms to removal by protons is crucial for the behavior of the OH abundances with varying metallicity and ionization parameter, as we describe in detail in §5 and §6.

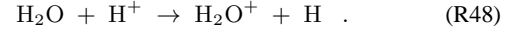
In addition to OH, the dissociative recombination of H₃O⁺ yields H₂O molecules (reaction [R33]). At high metallicities the H₂O is removed by rapid reactions with metal species



but it is also removed by

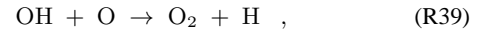


At low metallicity the H₂O is removed by

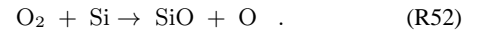
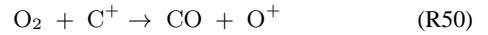
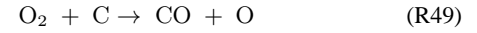


This is a removal mechanism for the H₂O (as is [R15] for OH) because some of the H₂O⁺ ions are removed by dissociative recombination rather than reentering the abstraction sequence that leads back to H₂O.

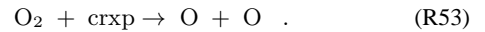
Following the formation of OH via [R14], [R27]–[R32], O₂ is produced by



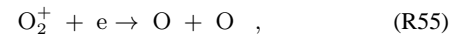
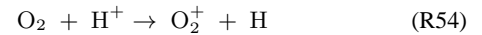
which as stated above is also the primary OH removal reaction at high metallicity. At high metallicity, the O₂ is removed by



The O₂ is also removed by internal photodissociation induced by secondary electron excitations of the H₂ (Sternberg et al. 1987; Gredel et al. 1989; Heays et al. 2014). Here and below, we refer to induced photodissociation with the label “crxp”. Thus,



At low metallicity, the O₂ is removed by protons in the sequence



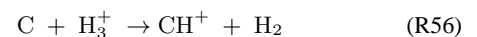
rather than by reactions with metal atoms and ions.

When any penetrating FUV radiation is present direct photodissociation and photoionization can become important in reducing the OH, H₂O, and O₂ abundances. We discuss the FUV photo-processes further in §2.4.

2.3 Carbon: CH and CO

Our carbon-oxygen network is shown in Figure 3. It includes C, C⁺, CH⁺, CH₂⁺, CH₃⁺, CH, CH₂, CO⁺, HCO⁺, and CO. We are mainly interested in the formation and destruction of CH and CO.

The production of CH is initiated by the formation of CH₂⁺ via proton transfer and abstraction



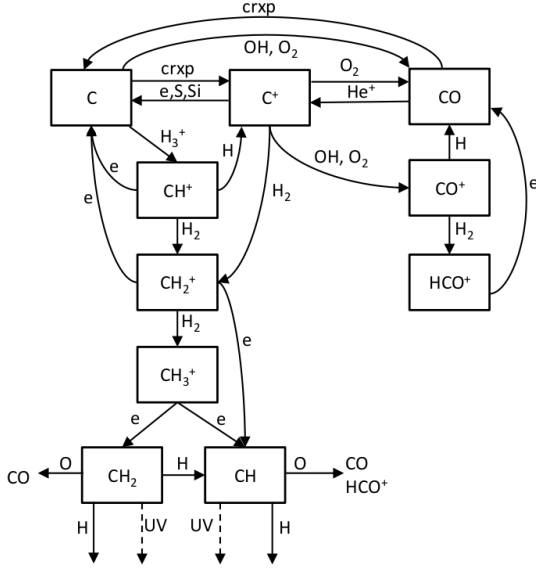
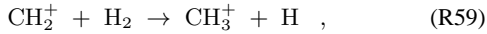


Figure 3. Formation-destruction pathways for CH and CO.

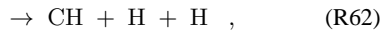
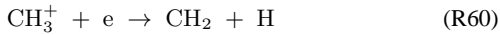
or by direct radiative association



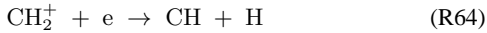
The relative efficiencies of [R56]-[R57] versus [R58] depend on the C^+/C ratio. The formation of CH_2^+ is followed by



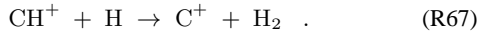
and then dissociative-recombination



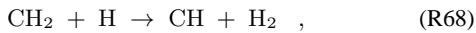
terminating in the production of CH (and CH_2). When the fractional ionization is large the abstraction sequence is moderated by



and

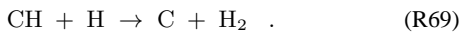


Reaction [R64] is an additional source of CH, but overall these moderating reactions tend to reduce the CH formation efficiency. When the e/H ratio is small



also contributes to CH formation.

In most of our parameter space, the dominant CH destruction reaction is

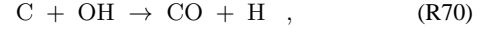


This, in contrast with OH, which is not removed by H atoms³. The destruction efficiency increases with the atomic hydrogen fraction,

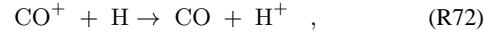
³ The binding energies of H_2 , OH, and CH are 4.48, 4.41 and 3.49 eV respectively. The reaction $\text{OH} + \text{H} \rightarrow \text{O} + \text{H}_2$ is exothermic, but it has a large

and CH therefore disappears as the metallicity is reduced. We discuss this further in §5 where we show that CH vanishes compared to OH as the metallicity is reduced.

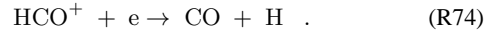
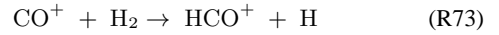
We now consider CO, which is produced via several channels. First is via OH,



or

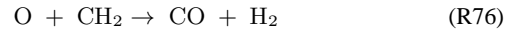
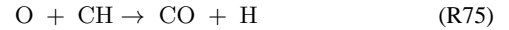


and

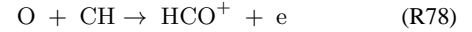


Reactions [R70]-[R74] are the CO production pathways via the “OH-intermediary”. For a given OH abundance, the relative efficiencies of these reactions depend on the C^+/C and H/H_2 density ratios. As we will discuss below, CO production via OH always dominates in the low Z' limit.

At sufficiently high Z' , the CH/OH ratio may become large (see §5.1), and CO is then also produced by

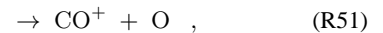
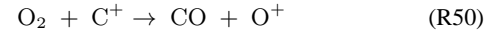


Another route is via chemionization



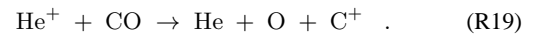
Reactions [R74]-[R78] are the CO production pathways via the “CH intermediary”. At sufficiently high metallicity (but mostly outside our parameter space) these reactions also contribute to the removal of the CH in addition to removal by H atoms.

CO formation can also proceed via



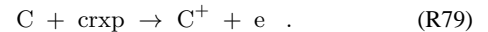
followed by [R72]-[R74]. These reactions are the CO production pathways via the “ O_2 intermediary”. As we discuss below, CO formation via O_2 becomes important at low ζ/n in the molecular regime where the O_2/OH abundance ratio can become large.

In the absence of FUV photodissociation, CO is destroyed mainly by dissociative charge transfer with He^+ ,



This is the primary CO removal mechanism at all metallicities.

Reaction [R19] is a major source of C^+ when much of the carbon is locked in CO, as occurs at high-metallicity. An additional source of C^+ , at all metallicities, is via crxp-ionization of any free carbon atoms



barrier (Balakrishnan 2004; van Dishoeck et al. 2013) and is ineffective in cold gas. $\text{CH} + \text{H} \rightarrow \text{C} + \text{H}_2$ is much more energetically favorable, and is rapid at low temperatures (Grebe & Homann 1982; Harding et al. 1993).

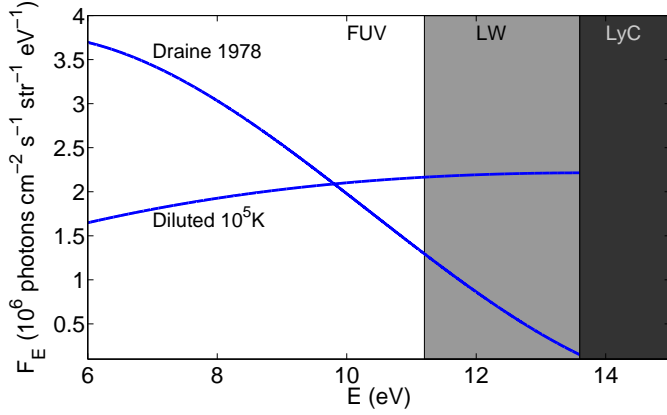
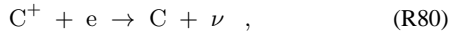
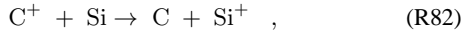


Figure 4. The Draine FUV spectrum and our diluted 10⁵ K black-body FUV spectrum, both for $I_{UV} = 1$ (see text). The light shaded region is the 11.2–13.6 eV LW band.

The C⁺ ions are removed by radiative recombination

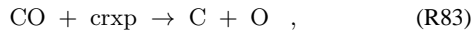


charge transfer

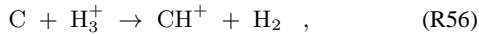


radiative association (reaction [R58]), and via the CO-forming reactions with OH or O₂ (reaction [R71] and [R50]–[R51]).

At high metallicity reactions [R81], [R82], and induced photodissociation



dominate the production of free atomic carbon. The carbon atoms are removed by induced ionization (reaction [R79]), by



and also by the CO-forming reactions with OH and O₂ (reactions [R70] and [R49]).

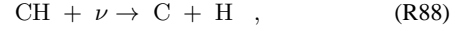
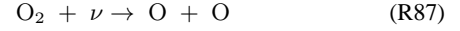
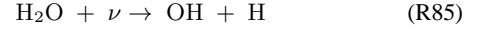
At low metallicity the C⁺/C ratio is set by the balance between induced photoionization [R79] and radiative-recombination [R80].

2.4 Photoprocesses

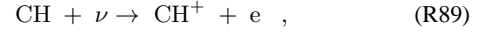
We also present computations including the effects of photodissociation and photoionization by externally incident FUV radiation. At very low metallicities, dust shielding may be ineffective, and photoprocesses will become significant in the presence of FUV. However, we assume that even at low Z' , the gas parcels are always shielded by H₂ gas columns $\gtrsim 10^{22} \text{ cm}^{-2}$ that completely block the 918–1108 Å LW band via fully overlapping H₂ absorption lines (e.g. Sternberg et al. 2014).

For such conditions, species such as C or CO with photodestruction thresholds within the LW band are fully shielded against the FUV. But for species with thresholds longward of 1108 Å, removal by FUV radiation can become important. This includes pho-

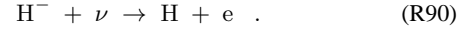
todissociation



photoionization



and photodetachment



We have used the photoprocess cross-sections in the van Dishoeck et al. (2006) database⁴ to calculate the dust-free photodissociation and photoionization rates for our species set assuming the Draine (1978, 2011) representation for the Galactic interstellar radiation field, as well as for a diluted 10⁵ K blackbody spectrum. For H[−] we used the photodetachment cross section calculated by Miyake et al. (2010, and H. Sadeghpour and P. Stancil, private communication). Computations of the H[−] photodetachment rate⁵ as a function of radiation temperature for blackbody spectra have also been presented by Latif et al. (2015).

We adopt the 10⁵ K spectrum as representative of the background FUV produced by massive Pop-III stars. We normalize the free-space fields by a scaling factor I_{UV} such that for $I_{UV} = 1$, the total photon density in the 6–13.6 eV band is $6.5 \times 10^{-3} \text{ cm}^{-3}$, as for the unit free space Draine field. The spectral shapes of the two normalized radiation fields are displayed in Figure 4. In Table 2 we assemble a selection of our computed list of photorates for $I_{UV} = 1$, for the Draine and the diluted blackbody fields assuming the LW-band is either optically thin or fully blocked (and with Lyman-continuum radiation always excluded). The photorates listed in Table 2 are the important b_{ij} factors that enter into our Equations (7) and (8) below.

3 RATE EQUATIONS

In our chemical computations we examine how the steady state abundances of atomic and molecular hydrogen, H and H₂, and heavy metal-bearing species, especially OH, H₂O, O₂, CH and CO, depend on the overall heavy element abundances as parameterized by the metallicity scaling factor Z' , and on the ionization parameter ζ/n . Here ζ is the total (primary plus secondary) H₂ ionization rate (s^{−1}), and $n \simeq n_H + 2n_{H_2}$ is the total volume density (cm^{−3}) of hydrogen nuclei in the gas parcels, where n_H and n_{H_2} are the atomic and molecular densities respectively. We assume that the parcels are exposed to steady sources of crx-ionization. We write the ionization rate as $\zeta = 10^{-16} \zeta_{-16} \text{ s}^{-1}$ where $\zeta_{-16} \approx 1$ is the characteristic Galactic value as inferred via H₃⁺ observations of clouds with H₂ column densities $\gtrsim 10^{21} \text{ cm}^{-2}$ (McCall et al. 2003, Indriolo & McCall 2012, Tielens 2013). We write the density $n = 10^3 n_3 \text{ cm}^{-3}$, where $n_3 \approx 1$ is the

⁴ <http://home.strw.leidenuniv.nl/~ewine/photo/>

⁵ Latif et al. presented H[−] photodetachment rates for $J_{21} = 1$, where J_{21} is the specific intensity in units of $10^{-21} \text{ erg s}^{-1} \text{ cm}^{-2} \text{ sr}^{-1} \text{ Hz}^{-1}$, at the Lyman limit. For a $T = 10^5 \text{ K}$ blackbody spectrum $I_{UV} = 182 J_{21}$, and our detachment rate of $2.7 \times 10^{-9} I_{UV} \text{ s}^{-1}$ is consistent with their result (see their Figure 1).

Table 2. Photorates for $I_{UV} = 1$

Reaction	Threshold (eV)	Photorate Γ (10^{-10} s^{-1})			
		Draine		Diluted 10^5 K	
		thin	LW-blocked	thin	LW-blocked
$\text{OH} + \nu \rightarrow \text{O} + \text{H}$	6.4	3.8	2.8	4.7	2.5
$\text{H}_2\text{O} + \nu \rightarrow \text{O} + \text{H}_2$	9.5	0.49	0.28	1.1	0.32
$\text{H}_2\text{O} + \nu \rightarrow \text{OH} + \text{H}$	6.0	7.5	5.5	11.7	4.8
$\text{O}_2 + \nu \rightarrow \text{O} + \text{O}$	7.0	7.9	7.0	9.4	5.1
$\text{CH} + \nu \rightarrow \text{C} + \text{H}$	3.4	9.0	8.8	5.5	4.7
$\text{CO} + \nu \rightarrow \text{C} + \text{O}$	11.5 ^a	2.6	0.0	14.2	0.0
$\text{C} + \nu \rightarrow \text{C}^+ + \text{e}$	11.3	3.2	0.0	10.1	0.0
$\text{CH} + \nu \rightarrow \text{CH}^+ + \text{e}$	3.4	7.7	0.97	21.3	1.4
$\text{H}^- + \nu \rightarrow \text{H} + \text{e}$	0.75 ^b	55.8	54.2	27.7	22.9

^a CO photodissociation occurs via absorption-line predissociation (Visser et al. 2009) and 11.5 eV is the lowest photon energy in this multiline process.

^b In computing the photodetachment rate we adopt the normalized Draine and diluted 10^5 K photon intensities from 13.6 eV all the way to the H^- electron detachment threshold of 0.75 eV.

characteristic density for star-forming molecular clouds in the Milky Way (McKee & Ostriker 2007). We adopt the chemical networks described in §2. We employ the reaction rate coefficients used by Boger & Sternberg (2005) which are based mainly on the UMIST99 database (Le Teuff et al. 2000) with some updates. The data compiled in UMIST12 (McElroy et al. 2013) or KIDA (Wakelam et al. 2012) do not differ significantly for our reaction networks, and we have verified by explicit computation that our results are insensitive to the data set used⁶.

For the gas phase heavy element abundances, we adopt the Asplund et al. (2009) solar photospheric values (Table 1), multiplied by the overall metallicity factor Z' , with no grain depletion factors at any Z' . (We keep the helium abundance constant at a cosmological value of 0.1). For H_2 formation on grains we assume a rate coefficient per hydrogen nucleus (Hollenbach et al. 1971; Jura 1974; Cazaux & Tielens 2002)

$$R = 3 \times 10^{-17} T_2^{1/2} Z'^{\beta} \text{ cm}^3 \text{ s}^{-1}, \quad (1)$$

where $T_2 \equiv T/100 \text{ K}$. The rate coefficient depends on the dust-to-gas ratio, and we assume that this varies as a power law, Z'^{β} , of the metallicity.

3.1 FUV off

In the absence of externally incident FUV radiation, the steady state densities, n_i (cm^{-3}), of the atomic and molecular species are determined by the set of formation-destruction rate equations,

$$\begin{aligned} & \sum_{jl} k_{ijl}(T) n_j n_l + \zeta \left[\sum_j a_{ij}^{\text{D}} n_j + x_{\text{H}_2} \sum_j a_{ij}^{\text{P}} n_j \right] \\ &= n_i \left\{ \sum_{jl} k_{jil}(T) n_l + \zeta \left[\sum_j a_{ji}^{\text{D}} + x_{\text{H}_2} \sum_j a_{ji}^{\text{P}} \right] \right\}. \quad (2) \end{aligned}$$

The $k_{ijl}(T)$ are the temperature dependent rate coefficients ($\text{cm}^3 \text{ s}^{-1}$) for two-body reactions of species j and l that lead to the formation of i . The a_{ij} are constants that multiply the total H_2 ionization rate ζ , and are divided into two parts. The a_{ij}^{D} are for direct

removal of species j by the energetic (ionizing) particles, leading to the production of i . The a_{ij}^{P} are for induced photodestruction (crxp) by the internal UV photons produced by secondary-electron excitations of the H_2 . The rates of the crxp processes are proportional to the H_2 gas density, and the a_{ij}^{P} are therefore multiplied by the H_2 fraction, $x_{\text{H}_2} \equiv n_{\text{H}_2}/n$.

The set of formation-destruction equations are augmented by mass and charge conservation. Thus,

$$\sum_i \alpha_{im} n_i = X_m n \quad (3)$$

where α_{im} is the number of atoms of element m contained in species i , and X_m is the total gas-phase abundance of element m relative to the hydrogen density n of nucleons. For the metals

$$X_m = A_m Z' \quad , \quad (4)$$

where A_m is the solar abundance of element m as given by Table 1. For helium we assume a constant cosmological abundance $A_{\text{He}} = 0.1$. Charge conservation is,

$$\sum_i q_i n_i = 0 \quad (5)$$

where q_i is the net charge of species i .

Dividing the rate equations by n^2 gives

$$\begin{aligned} & \sum_{jl} k_{ijl}(T) x_j x_l + \frac{\zeta}{n} \left[\sum_j a_{ij}^{\text{D}} x_j + x_{\text{H}_2} \sum_j a_{ij}^{\text{P}} x_j \right] \\ &= x_i \left\{ \sum_{jl} k_{jil}(T) x_l + \frac{\zeta}{n} \left[\sum_j a_{ji}^{\text{D}} + x_{\text{H}_2} \sum_j a_{ji}^{\text{P}} \right] \right\}, \quad (6) \end{aligned}$$

where $x_i \equiv n_i/n$ are the fractional abundances of species i relative to the total hydrogen gas density. This shows that for a given Z' (and with $X_m = A_m Z'$ for the metals) and for a given gas temperature, the fractional abundances depend only on the ionization parameter ζ/n (e.g., Lepp & Dalgarno 1996; Boger & Sternberg 2005). We consider isothermal gas, and thus the two basic parameters in our study are ζ/n and the metallicity Z' .

The rate equations are non-linear, and we solve them iteratively using Newton's method.

⁶ An exception is the position of the LIP/HIP boundary (see below) which can be sensitive to small rate-coefficient variations.

3.2 FUV on

In the presence of externally incident FUV radiation (§2.4) photodissociation and photoionization processes must be added to the formation-destruction equations. These are then,

$$\begin{aligned} \sum_{jl} k_{ijl}(T) n_j n_l + \zeta \left[\sum_j a_{ij}^D n_j + x_{H_2} \sum_j a_{ij}^P n_j \right] \\ + I_{UV} \sum_j b_{ij} = n_i \left\{ \sum_{jl} k_{jil}(T) n_l \right. \\ \left. + \zeta \left[\sum_j a_{ji}^D + x_{H_2} \sum_j a_{ji}^P \right] + I_{UV} \sum_j b_{ji} \right\}. \quad (7) \end{aligned}$$

The $b_{ij} I_{UV}$ in the additional terms are the photodissociation or photoionization rates (s^{-1}) of species j that produce i (Table 2). Dividing by n^2 we have,

$$\begin{aligned} \sum_{jl} k_{ijl}(T) x_j x_l + \frac{\zeta}{n} \left[\sum_j a_{ij}^D x_j + x_{H_2} \sum_j a_{ij}^P x_j \right] \\ + \frac{I_{UV}}{n} \sum_j b_{ij} x_j = x_i \left\{ \sum_{jl} k_{jil}(T) x_l \right. \\ \left. + \frac{\zeta}{n} \left[\sum_j a_{ji}^D + x_{H_2} \sum_j a_{ji}^P \right] + \frac{I_{UV}}{n} \sum_j b_{ji} \right\}. \quad (8) \end{aligned}$$

When FUV radiation is present a third parameter enters, I_{UV}/n , the ratio of the FUV intensity to the gas density. Here I_{UV} refers to the local FUV intensity inside the gas parcel, after accounting for any shielding by an outer dust-absorption layer.

We assume that the LW band is always fully blocked by a shielding H₂ gas column of at least 10^{22} cm^{-2} . For such shielding columns FUV photodissociation is always negligible compared to crx-ionization of the H₂ in the gas parcels. To keep the cloud sizes reasonably small we assume that the column densities of any photodissociated atomic (HI) envelopes are negligible compared to the H₂ shielding columns, even at very low Z' . This requires that

$$n \gtrsim 2 \times \frac{I_{UV}^0}{Z'^\beta} \text{ cm}^{-3}, \quad (9)$$

where I_{UV}^0 is the free-space FUV radiation intensity factor. This follows from the Sternberg et al. (2014) expression for the photodissociated HI column in the “weak field” limit ($I_{UV}^0/n_3 \lesssim 10$), and given by $N_{HI} \approx 0.1 F_0 / (2 R n) = 4 \times 10^{19} Z'^{-\beta} (I_{UV}^0/n_3) \text{ cm}^{-2}$. In this expression, $F_0 = 2.07 \times 10^7 \text{ cm}^{-2}$ is the characteristic photodissociation photon flux for $I_{UV}^0 = 1$ (Draine 2003; Sternberg et al. 2014). For $\beta = 1$ and $I_{UV}^0 = 1$ Equation (9) requires $n \gtrsim 2 \times 10^3 \text{ cm}^{-3}$ for $Z' = 10^{-3}$. The corresponding cloud sizes including the shielding envelopes are then $\lesssim 10 \text{ pc}$.

For an LW H₂ blocking column $N_{H_2}^{\text{block}} = 10^{22} \text{ cm}^{-2}$ the associated 1000 Å dust opacity is $\tau_g = 2\sigma_g N_{H_2}^{\text{block}} \approx 38 Z'^\beta$, where $\sigma_g = 1.9 \times 10^{-21} Z'^\beta \text{ cm}^2$ is the dust cross-section per hydrogen nucleon. Thus when turning on the FUV field in Equations (7) and (8), we set

$$I_{UV} = I_{UV}^0 e^{-\tau_g} = I_{UV}^0 e^{-38 Z'^\beta}, \quad (10)$$

In this expression we are assuming that the dust opacity associated with any HI in the shielding layer is negligible.

Our expression for I_{UV} allows the local field intensity inside the parcels to vary smoothly as we vary Z' , and as the effects of

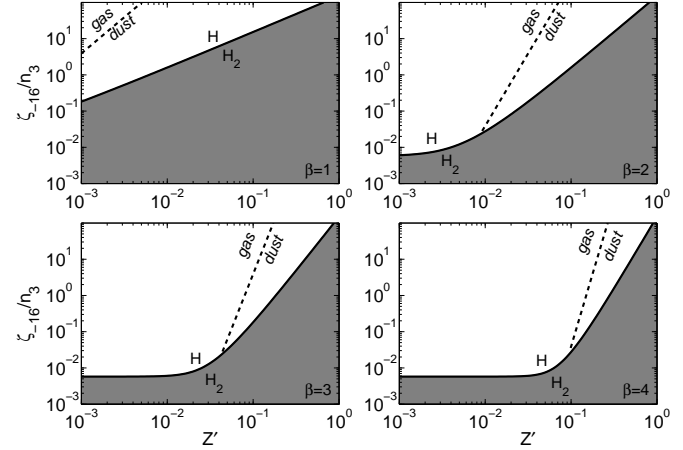


Figure 5. Atomic (H) and molecular (H₂) regimes in the ζ_{-16}/n_3 versus Z' parameter space, assuming $R = R_0 Z'^\beta$, for $\beta=1, 2, 3$ and 4 (see text). The solid curves are the H-to-H₂ transition lines where $n_H = n_{H_2}$. The hydrogen is molecular below the solid curves (shaded) and atomic above them. In the atomic regimes, the dashed lines separate the zones where gas-phase versus dust catalysis dominate the H₂ formation.

dust shielding are altered. For simplicity, and because we are assuming an arbitrary shielding column, we ignore the wavelength dependence of the dust attenuation for the individual species in our set. For high enough Z' , the dust opacity becomes large and all of the photorates vanish due to significant dust shielding. When the metallicity is low, τ_g is small, but the LW band remains blocked. Species that are removed by $\lambda > 1108 \text{ Å}$ photons are only partially shielded, or not at all for sufficiently small Z' .

4 H/H₂ BALANCE ANALYTIC TREATMENT, AND TIME SCALES

Before presenting our detailed chemical computations (in §5 and §6) we consider just H₂ formation-destruction and the behavior of the H/H₂ density ratio, in a simplified analytic treatment, showing the dependence on ζ/n and Z' . Our analysis generalizes previous discussions (e.g., de Jong 1972; Glover 2003; Cazaux & Spaans 2004). We also consider the dependences of the H₂ formation time-scales on Z' and ζ/n . The H₂ formation time-scales determine the overall conditions required for chemical equilibrium.

4.1 Steady State H/H₂

As discussed in §2.1 the two primary H₂ formation channels are grain catalysis (reaction [R1]) and gas phase production via H[−] ([R2] and [R3]). In the absence of FUV photodissociation, the H₂ is removed by crx-ionization (reactions [R8] and [R7]) leading mainly to the formation of H₂⁺. When the gas is primarily molecular, the destruction rate is *enhanced* by further reactions of the H₂ with H₂⁺ (reaction [R9]). However, when the gas is atomic the net H₂ removal rate is *reduced* by electron charge transfer from H to H₂⁺, leading back to H₂ (reaction [R6]).

Thus, the H/H₂ formation-destruction equation for steady state conditions is

$$\zeta \times y \times f_d \times n_{H_2} = [Rn + k_2 n_e] n_H, \quad (11)$$

with

$$2n_{\text{H}_2} + n_{\text{H}} = n \quad , \quad (12)$$

or

$$\left(\frac{\zeta}{n}\right) \times y \times f_d \times x_{\text{H}_2} = [R + k_2 x_e] x_{\text{H}} \quad , \quad (13)$$

with

$$2x_{\text{H}_2} + x_{\text{H}} = 1 \quad . \quad (14)$$

Here n_{H} and n_{H_2} , and x_{H} and x_{H_2} , are the atomic and molecular hydrogen densities and fractions, ζ is the crx-ionization rate, and R is the grain-surface H_2 formation rate coefficient. The rate coefficient $k_2 = 2.0 \times 10^{-16} T_2^{0.67} \text{ cm}^3 \text{ s}^{-1}$ (independent of Z') is for radiative association of hydrogen atoms with electrons (reaction [R2]) which is the rate limiting step for gas-phase H_2 formation. On the left-hand side, the factor $y \simeq 2$ in the molecular regime ($2x_{\text{H}_2} \simeq 1$) where the H_2 destruction rate is enhanced by the further reactions with H_2^+ . In the atomic regime ($x_{\text{H}} \simeq 1$) the parameter $y \simeq 1$. The factor f_d is the fraction

$$f_d \equiv \frac{k_{R9} x_{\text{H}_2}}{k_{R9} x_{\text{H}_2} + k_{R6} x_{\text{H}}} \quad , \quad (15)$$

of all H_2 ionizations that are not followed by charge-transfer back to H_2 . In the molecular regime $f_d \simeq 1$. In the atomic regime $f_d \simeq 3.3x_{\text{H}_2}/x_{\text{H}}$.

In this analysis we assume that the dust-to-gas ratio varies as a power β of the metallicity as given by Equation (1), and write

$$R = R_0 Z'^{\beta} \quad , \quad (16)$$

where $R_0 = 3 \times 10^{-17} T_2^{1/2} \text{ cm}^3 \text{ s}^{-1}$ is the rate coefficient for solar ($Z'=1$) metallicity. (In our full chemical computations in §5 and §6 we set $\beta = 1$).

In Equation (13), the gas phase formation term, $k_2 x_e$, can become important only when the hydrogen is primarily atomic since then a relatively large H^- abundance can be maintained by electron attachment. We estimate x_e in the atomic-regime via the condition of ionization-recombination equilibrium

$$0.46\zeta n_{\text{H}} \simeq 0.46\zeta n = \alpha_B n_{\text{H}} + n_e \simeq \alpha_B n_e^2 \quad , \quad (17)$$

or

$$\begin{aligned} x_e \equiv \frac{n_e}{n} &\simeq 0.68 \left(\frac{\zeta}{\alpha_B n}\right)^{1/2} \\ &= 7.6 \times 10^{-5} T_2^{0.38} \left(\frac{\zeta_{-16}}{n_3}\right)^{1/2} \quad . \end{aligned} \quad (18)$$

Here we have assumed $\alpha_B = 8.0 \times 10^{-12} T_2^{-0.75} \text{ cm}^3 \text{ s}^{-1}$ for case B radiative recombination.

Given expressions (16) and (18) for R and x_e , and setting $x_{\text{H}} = x_{\text{H}_2}$ in Equation (13), we obtain the relation between ζ/n and Z' for which the atomic and molecular densities are equal. These are the solid curves in Figure 5, for $\beta=1, 2, 3$, and 4, and assuming $T_2 = 1$.

For any β , the curves flatten when Z' is sufficiently small and gas-phase H_2 formation dominates. In this limit Rn is negligible in Equation (13), and for $x_{\text{H}} = x_{\text{H}_2}$

$$f_d \times y \times \frac{\zeta}{n} = k_2 x_e \quad . \quad (19)$$

Assuming $y = 2$, $f_d = 1$ at the H-to- H_2 transition point (justified by the results of our detailed numerical solutions), and assuming

Equation (18) for the fractional ionization, the ionization parameter for which $x_{\text{H}} = x_{\text{H}_2}$ is given by

$$\frac{\zeta}{n} \simeq 0.12 \frac{k_2^2}{\alpha_B} \quad . \quad (20)$$

Thus for gas-phase H_2 formation (low Z' limit), the atomic-to-molecular transition occurs at

$$\frac{\zeta_{-16}}{n_3} \simeq 5.7 \times 10^{-3} T_2^{2.1} \quad , \quad (21)$$

as seen in Figure 5 for very low Z' .

At sufficiently high Z' , grain H_2 catalysis dominates, the H_2 formation efficiency increases as Z'^{β} , and the H/ H_2 transition curves turn upward. Then, neglecting the gas phase formation term $k_2 n_e$ in Equation (13), and again setting $y = 2$ and $f_d = 1$ we have

$$\frac{\zeta}{n} \simeq 0.5 R_0 Z'^{\beta} \quad . \quad (22)$$

This gives

$$\frac{\zeta_{-16}}{n_3} \simeq 1.5 \times 10^2 T_2^{1/2} Z'^{\beta} \quad (23)$$

for the H/ H_2 transition curves for H_2 grain catalysis. For example, for $\beta = 2$, the H-to- H_2 transition occurs at $\zeta_{-16}/n_3 = 1.5 T_2^{1/2}$ for $Z' = 0.1$, or at $\zeta_{-16}/n_3 = 1.5 \times 10^2 T_2^{1/2}$ for $Z' = 1$.

In Figure 5, the dashed lines delineate the zones where gas-phase production (to the left) versus grain catalysis (to the right) dominates H_2 formation in the atomic regimes ($x_{\text{H}} \simeq 1$) above the solid curves. We draw these by equating the two formation rates

$$R_0 Z'^{\beta} = x_e k_2 \quad (24)$$

and using Equation (18) for x_e . This gives

$$\frac{\zeta}{n} = 2.2 \left(\frac{R_0 Z'^{\beta}}{k_2}\right)^2 \alpha_B \quad , \quad (25)$$

or

$$\frac{\zeta_{-16}}{n_3} = 4.0 \times 10^6 T_2^{-1.1} Z'^{2\beta} \quad , \quad (26)$$

for the dashed lines in Figure 5. For example, for $\beta = 2$ the gas phase and grain H_2 formation rates are equal for $\zeta_{-16}/n_3 = 4 \times 10^{-2} T_2^{-1.1}$ for $Z' = 10^{-2}$, or $\zeta_{-16}/n_3 = 4 \times 10^2 T_2^{-1.1}$ for $Z' = 0.1$.

We may now define the critical metallicity Z'_{crit} at which the gas-phase and dust-grain formation rates are equal at the H-to- H_2 transition point. For $Z' < Z'_{\text{crit}}$ the H-to- H_2 transition is controlled by the gas-phase formation. For $Z' > Z'_{\text{crit}}$ dust-formation dominates the transition. The critical metallicities occur at the intersections of the dashed and solid curves in Figure 5. These intersections may be estimated by equating Equations (21) and (23). This gives

$$Z'_{\text{crit}}^{\beta} \simeq 0.23 \frac{k_2^2}{2 \times \alpha_B R_0} = 3.8 \times 10^{-5} T_2^{1.6} \quad . \quad (27)$$

For β increasing from 1 to 4, Z'_{crit} ranges from $4 \times 10^{-5} T_2^{1.1}$ to $8 \times 10^{-2} T_2^{1.6}$.

Finally, expressions for the H_2 fraction in the atomic regime ($x_{\text{H}} \simeq 1$) may now be written down. For gas-phase formation, Equation (13) takes the form

$$\frac{x_{\text{H}_2}}{x_{\text{H}}} \simeq k_2 x_e \frac{1}{f_d} \frac{1}{y} \left(\frac{\zeta}{n}\right)^{-1} \quad . \quad (28)$$

Setting $y = 1$ and $f_d \simeq 3.25x_{\text{H}_2}/x_{\text{H}}$ as appropriate for the atomic regime, and using Equation (18) for the electron fraction, we obtain

$$x_{\text{H}_2} \simeq \frac{x_{\text{H}_2}}{x_{\text{H}}} \simeq 0.22 T_2^{0.5} \left(\frac{\zeta_{-16}}{n_3} \right)^{-1/4}. \quad (29)$$

For dust catalysis

$$\frac{x_{\text{H}_2}}{x_{\text{H}}} \simeq R_0 Z'^{\beta} \frac{1}{f_d} \frac{1}{y}, \quad (30)$$

and

$$x_{\text{H}_2} \simeq \frac{x_{\text{H}_2}}{x_{\text{H}}} \simeq 0.95 T_2^{1/4} \left(\frac{\zeta_{-16}}{n_3} \right)^{-1/2} \left(\frac{Z'}{10^{-2}} \right)^{\beta/2}. \quad (31)$$

Where again we set $y = 1$ and $f_d \simeq 3.25x_{\text{H}_2}/x_{\text{H}}$ as appropriate for the atomic regime.

4.2 Time Scales

In the analysis above and in our computations in §5 and §6 we are assuming that the systems are in a steady state, and that the chemical equilibrium times are shorter than the cloud lifetimes. Overall equilibrium is set by the relatively long time-scale for H₂ formation. For grain catalysis the H₂ formation time scale is

$$t_{\text{H}_2}^{\text{dust}} = \frac{1}{Rn} \approx 10^6 T_2^{-1/2} n_3^{-1} Z'^{-\beta} \text{ yr}. \quad (32)$$

For the gas phase formation via H⁺ the time scale is

$$t_{\text{H}_2}^{\text{gas}} = \frac{1}{k_2 n x_e} \approx 2 \times 10^9 T_2^{-1.1} n_3^{-1/2} \zeta_{-16}^{-1/2} \text{ yr}, \quad (33)$$

where we used Equation (18) for x_e . The ratio of these time scales is

$$\frac{t_{\text{H}_2}^{\text{dust}}}{t_{\text{H}_2}^{\text{gas}}} = \frac{k_2 n x_e}{Rn} \approx 5 \times 10^{-4} T_2^{0.6} \left(\frac{\zeta_{-16}}{n_3} \right)^{1/2} \frac{1}{Z'^{\beta}}. \quad (34)$$

At solar ($Z' = 1$) metallicity, H₂ formation on dust is much faster than in the gas-phase unless the gas density is unusually low, or the ionization parameter is extremely large. At low Z' and low dust-to-gas ratios, the gas phase formation route may become faster even at characteristic densities. Both time-scales are generally short compared to the present day age of the universe (13.8 Gyr), and the typical ages of galaxies, and H₂ formation is rapid for shielded gas. However, at the early reionization epoch ($z \approx 10$, or 0.48 Gyr, Hinshaw et al. 2013), the H₂ formation time-scale may become long irrespective of the cloud evolution time scales. For example, at reionization, and an early metal abundance $Z'=10^{-3}$ but for a Galactic $\zeta_{-16}/n_3 = 1$, the dust and gas-phase H₂ formation time-scales are comparable even for $\beta = 1$. A large cloud density, $n \gtrsim 2 \times 10^3 \text{ cm}^{-3}$, is then required to achieve a chemical steady state, for complete conversion of H to H₂ within the corresponding Hubble time.

5 ANALYSIS AND SCALING RELATIONS

With the above analytic results for the steady-state H/H₂ balance and time scales, we now show full chemical computations for several illustrative model sequences, as one-dimensional (1D) cuts through our parameter space. We first present models for varying Z' at fixed ζ/n , and second for varying ζ/n at fixed Z' . In all of these computations we assume that the H₂ formation rate coefficient varies linearly with Z' (i.e., we set $\beta=1$ in Equation [1]), and

solve Equations (3)-(6) and (8) for our chemical networks, with-out and with FUV. For FUV on we assume the photorates for the diluted 10^5 K radiation field (see Table 2).

5.1 Dependence on Z' for fixed ζ/n .

In Figure 6 we display the steady-state abundances, $x_i \equiv n_i/n$, for H, H₂, H⁺, e, C, O, OH, H₂O, O₂, CH and CO. In these computations we set $\zeta_{-16}/n_3 = 1$, and vary Z' from 1 to 10^{-3} . Again, we are assuming that the LW band is always blocked so that H₂ and CO photodissociation is always excluded whether or not an FUV background field is present.

The upper left panel shows the behavior for H and H₂. For $Z' \gtrsim 10^{-2}$, H₂ formation by dust-grain catalysis is rapid compared to H₂ removal by crx-ionization, and the gas is fully molecular. The atomic hydrogen fraction increases as grain H₂ formation becomes less efficient with decreasing Z' according to Equation (1). The H-to-H₂ transition occurs at $Z' \approx 10^{-2}$, and this is consistent with Equation (23) for $\zeta_{-16}/n_3=1$. The H₂ abundance continues to drop as Z' is reduced and as the molecular formation efficiency decreases. The curve for x_{H_2} finally flattens as Z' becomes very small and gas-phase formation dominates, however this occurs only for $Z' < 10^{-3}$ below the minimum Z' that we consider.

The upper-right panel of Figure 6 shows the electron fraction x_e . It also shows the summed fractions of the metal positive charge carriers. For our assumed $\zeta_{-16}/n_3 = 1$, these are mainly the atomic ions C⁺, Si⁺, and S⁺. The metal positive charge carriers are collectively labeled “metal-ions” in Figure 6. This panel also shows the proton fraction x_{H^+} . In general, the interstellar gas-phase chemical sequences yield two types of solutions (HIP and LIP) for the equilibrium ionization states, depending on ζ/n and the gas-phase elemental abundances (Oppenheimer & Dalgarno 1974; Pineau des Forets et al. 1992; Le Bourlot et al. 1993; Lee et al. 1998; Boger & Sternberg 2006; Wakelam et al. 2006). In the “high-ionization-phase” (HIP) the electrons are removed by a combination of H₃⁺ dissociative recombination and radiative recombination of the atomic metal ions. In the “low-ionization-phase” (LIP) the electrons are removed mainly by dissociative recombination with molecular metal ions. In purely gas-phase systems the HIP to LIP transition can be abrupt due to instabilities in the chemical networks (e.g. Boger & Sternberg 2006). The model sequence in Figure 6 is all HIP for the full range of Z' for our assumed $\zeta_{-16}/n_3=1$.

At $Z'=1$, $x_e \simeq 5 \times 10^{-5}$ and the positive charge is carried by the metal ions. As Z' is reduced the total metal ion fraction drops linearly, and x_e decreases accordingly. Meanwhile, the proton fraction rises with the increasing abundance of free hydrogen atoms available for direct crx-ionization (reaction [R13]). The decreasing metal-ion densities together with the increasing abundance of protons leads to the minimum $x_e \simeq 6 \times 10^{-6}$ at $Z' \approx 4 \times 10^{-2}$. At very low Z' , H⁺ becomes the dominant positive charge carrier, and x_e increases until the gas becomes fully atomic. He⁺ does not contribute significantly because it is rapidly removed by charge transfer (reactions [R19]-[R22]). In the fully atomic regime the electron fraction reaches a plateau of $x_e \approx 7 \times 10^{-5}$, consistent with Equation (18) for the balance between hydrogen ionization and electron-proton radiative recombination.

The middle-left panels of Figure 6 show the abundance fractions x_i versus Z' , for C, O, OH, H₂O, O₂, CH, and CO, for FUV off. These fractions are relative to the total hydrogen gas density. In the lower-left panels we normalize relative to the total available oxygen or carbon at each Z' , and plot curves for C/C_{tot}, CH/C_{tot}, CO/C_{tot}, O/O_{tot}, OH/O_{tot}, H₂O/O_{tot}, and O₂/O_{tot},

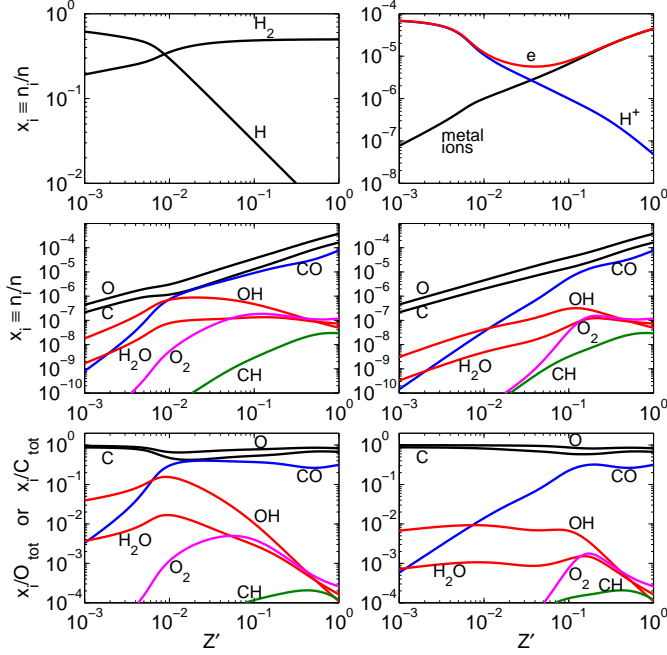


Figure 6. Abundances versus metallicity for $\zeta_{-16}/n_3=1$ and $T_2=1$. The upper and middle panels show abundances relative to total hydrogen nuclei, $x_i \equiv n_i/n$ ($n = n_H + 2n_{H_2}$). In the bottom panels we normalize to the total elemental carbon and oxygen abundances ($C_{\text{tot}} = 2.9 \times 10^{-4} Z'$ and $O_{\text{tot}} = 4.9 \times 10^{-4} Z'$). In the lower right panel $I_{UV}^0/n_3=1$, in all other panels $I_{UV}^0/n_3=0$.

(where $O_{\text{tot}} \equiv A_O Z' = 4.9 \times 10^{-4} Z'$ and $C_{\text{tot}} \equiv A_C Z' = 2.9 \times 10^{-4} Z'$).

Several important features and trends can be seen. First, at high Z' , the dominant metal-bearing molecule is CO. For example for $Z' \approx 1$, $x_{\text{CO}} \approx 8 \times 10^{-5}$ and $\text{CO}/C_{\text{tot}} \approx 0.3$. When the hydrogen is molecular ($Z' \gtrsim 10^{-2}$), at least 30% of the available carbon is locked in CO with the remaining carbon in atomic form. Because $O_{\text{tot}}/C_{\text{tot}} > 1$ in our models a large fraction of the oxygen always remains atomic. The large CO abundance is the familiar chemical state for standard interstellar molecular clouds. Figure 6 shows that CO production is efficient at all Z' so long as the hydrogen is molecular. In the absence of selective photodissociation the CO then serves as a good proxy for the H_2 (e.g. Bolatto et al. 2013). We refer to this limit as the “CO-dominated regime”. When the hydrogen is atomic ($Z' \lesssim 10^{-2}$ for $\zeta_{-16}/n_3 = 1$) the CO abundance drops sharply and then OH becomes the most abundant molecule containing a heavy element. We refer to this limit as the “OH-dominated” regime. Figure 6 shows that the transition from the OH to CO dominated regimes occurs close to the H-to- H_2 transition point. As we discuss further below this is true for any ζ/n . A large atomic carbon abundance is generally maintained when ζ/n is sufficiently large for a given Z' , and the C/CO density ratio is then of order of unity. At low ζ/n the C/CO ratio always becomes small. In Figure 6 we are in the large ζ/n regime.

Second, the OH, H_2O , O_2 , and CH abundances are all comparable for large Z' . For our assumed $\zeta_{-16}/n_3=1$, x_{OH} , x_{H_2O} , x_{O_2} , and x_{CH} are $\sim 10^{-8}$ at $Z' = 1$, as seen in Figure 6. However, the abundance curves for these four species diverge sharply as Z' becomes small.

The behavior for OH is of particular interest. As Z' is reduced, the OH abundance first *increases*, and reaches a maximum near the

H/ H_2 transition. At this point, $x_{\text{OH}} = 6 \times 10^{-7}$, and $\text{OH}/O_{\text{tot}} = 0.16$, and a significant fraction of the gas phase oxygen is locked in OH molecules. In particular, the OH/CO abundance ratio ~ 1 at this point. At still lower Z' the OH abundance decreases, but once the hydrogen becomes predominantly atomic OH/ O_{tot} approaches a constant value of 2%. In contrast, CO/C_{tot} decreases linearly with Z' , and OH/CO becomes large.

The variation of x_{OH} with Z' and ζ/n is essential and can be understood via an approximate analytic scaling relation, as follows. (We show numerical results for x_{OH} versus ζ/n at fixed Z' in §5.2). At high Z' , and in the molecular regime ($2x_{H_2} \simeq 1$), ionization of H_2 leads to the formation of H^+ or H_3^+ that then react with atomic oxygen (reactions [R14] and [R28]) initiating the abstraction sequence leading to OH. At temperatures $\gtrsim 50$ K the H^+ density is limited by charge transfer with atomic oxygen (reaction [R14]). The OH formation rate via H^+ is then equal to the dissociative H_2 ionization rate, and independent of metallicity. For the HIP conditions in Figure 6 the H_3^+ density is limited by dissociative recombination ([R10] and [R11]). The relative rates of the H^+ versus H_3^+ routes therefore depends on the atomic oxygen to electron ratio. The OH is removed mainly by atomic oxygen (reaction [R39]) hence the removal rate is proportional to Z' , and independent of ζ/n . To a good approximation we then have

$$x_{\text{OH}} \propto \left(\frac{\zeta}{n}\right) \left[1 + \frac{0.93k_{R28}}{0.02(k_{R10} + k_{R11})} \frac{x_O}{x_e} \right] \frac{1}{Z'} \\ = \left(\frac{\zeta}{n}\right) \left[1 + 0.27 \frac{x_O}{x_e} \right] \frac{1}{Z'} \quad , \quad (35)$$

where k_{R28} , k_{R10} , k_{R11} are the rate coefficients for reactions [R28], [R10] and [R11] (evaluated for $T_2 = 1$), and the terms in brackets account for the H^+ and H_3^+ formation channels respectively. To first-order, x_{OH} is proportional to ζ/n , and for a given hydrogen gas density the OH abundance is a measure of the ionization rate (e.g., Black & Dalgarno 1973; van Dishoeck & Black 1986). In Equation (35), the H^+ formation channel dominates when the oxygen-to-electron ratio, x_O/x_e , is small. The oxygen-to-electron ratio is independent of Z' when the positive charge is carried by metal species as is the case for high Z' , but it does vary inversely with ζ/n and this moderates the sensitivity of x_{OH} to ζ/n (as discussed further in §5.2). To first order the OH formation rate is independent of metallicity. The $1/Z'$ term in Equation (35) accounts for the removal of the OH by atomic oxygen. Figure 6 shows the approximately linear rise in x_{OH} as the metallicity is reduced.

In the opposite limit; low Z' , atomic regime ($x_H \simeq 1$), and for gas-phase H_2 production, OH formation proceeds via reactions of O^+ ions with the trace H_2 available (reaction [R27]). But now the O^+ density is set by charge transfer equilibrium with atomic hydrogen (reaction [R14]), and the H^+ is removed by electron recombination. Thus, in this limit the OH formation rate is linearly proportional to the oxygen abundance and metallicity. Removal of the OH is via reactions with H^+ [R43] rather than by oxygen and other metals. In this limit

$$x_{\text{OH}} \propto x_{H_2} \frac{1}{f} \frac{x_{O^+}}{x_{H^+}} \propto x_{H_2} \frac{1}{f} \frac{x_O}{x_H} \propto x_{H_2} \frac{1}{f} Z' \quad . \quad (36)$$

Here $f \propto x_e/x_{H_2}$ is the fraction of OH^+ productions (via [R43]) that do not loop back to OH via the abstraction sequence [R29]–[R32]. In Equation (36), $x_{O^+}/x_{H^+} \propto x_O/x_H$ as set by forward and backward charge-transfer equilibrium. Furthermore, from Equations (13) and (18), we have $x_e \propto (\zeta/n)^{1/2}$ and $x_{H_2} \propto$

$(\zeta/n)^{-1/4}$. Thus at low Z' , x_{OH} is proportional to Z' , and

$$x_{\text{OH}} \simeq 0.02 A_{\text{O}} Z' \left(\frac{\zeta_{-16}}{n_3} \right)^{-1}, \quad (37)$$

where $A_{\text{O}} = 4.9 \times 10^{-4}$ is the oxygen abundance at solar metallicity. In expression (37) the prefactor of 2% is obtained from our numerical results, as shown in Figure 6. Importantly, the OH fraction varies *inversely* with ζ/n in the low Z' limit. This is due to (a) the reduced H₂ fraction with increasing ionization parameter, and (b) the increased electron to H₂ ratio that enhances the efficiency of OH destruction by protons.

The behavior for H₂O and O₂ differs due to the variety of removal processes with metal atoms and ions, [R44]–[R47] for H₂O, and [R49]–[R53] for O₂. At high Z' , the H₂O and O₂ removal rates are weakly dependent on Z' as the relative fractions of C, C⁺, Si, and Si⁺ vary. The overall abundances of these atoms and ions increase with ζ/n and therefore so do the H₂O and O₂ removal rates. The H₂O formation rate is independent of Z' to first order, as for OH. For O₂ the formation rate is proportional to the product of the OH and O densities, and this is also independent of Z' . However, the formation rates increase with ζ/n . Thus, in the high Z' regime we expect that $x_{\text{H}_2\text{O}}$ and x_{O_2} will be insensitive to both Z' and ζ/n . As seen in Figure 6, $x_{\text{H}_2\text{O}}$ and x_{O_2} are indeed roughly constant from $Z' = 1$ down to 0.05. We show results as functions of ζ/n in Figures 7 and 8 below.

At lower Z' , and into the atomic regime, the H₂O and O₂ are both removed by H⁺. In the low Z' atomic limit,

$$x_{\text{H}_2\text{O}} \simeq 2 \times 10^{-3} A_{\text{O}} Z' \left(\frac{\zeta_{-16}}{n_3} \right)^{-1}, \quad (38)$$

and

$$x_{\text{O}_2} \simeq 3 \times 10^{-3} A_{\text{O}} Z'^2 \left(\frac{\zeta_{-16}}{n_3} \right)^{-1.5}. \quad (39)$$

The H₂O fraction depends on the ionization parameter in the same way as OH does, and for identical reasons. For x_{O_2} , the dependence is steeper, with one power of ζ/n entering due to the formation via OH, and an additional $(\zeta/n)^{1/2}$ term for the proton fraction that controls the removal rate.

In the low Z' limit x_{OH} and $x_{\text{H}_2\text{O}}$ are proportional to Z' because both OH and H₂O contain just one heavy element. However, $x_{\text{O}_2} \propto Z'^2$ because O₂ consists of two heavy elements. These simple metallicity scalings are inevitable when the heavy molecules are removed only by hydrogen-helium species and once the hydrogen-helium chemistry and the electron fraction are no longer affected by metals (or dust), as occurs at sufficiently low Z' for any ζ/n (or for sufficiently high ζ/n for any Z'). In this limit, and for any network of two-body reactions, the abundances of any *trace* species containing n heavy elements must always vary as Z'^n . Our numerical calculations are consistent with this general principle. Thus O₂ vanishes compared to OH in the low Z' limit, as does CO compared to OH as we discuss further below.

In the molecular regime the H₂O/OH abundance ratio is variable and can become large. In the atomic regime, H₂O/OH is always small, ~ 0.1 , (and constant) because the H₂O removal rate by H⁺ is larger than for OH, and because most H₃O⁺ ions dissociatively recombine to OH rather than to H₂O (e.g., Vejby-Christensen et al. 1997).

Figure 6 shows that OH/CH is a strongly decreasing function of Z' , even though the total oxygen to carbon abundance ratio, $O_{\text{tot}}/C_{\text{tot}}$, is independent of Z' in our models. In particular, CH vanishes with decreasing Z' . This occurs because for all $Z' \lesssim 1$,

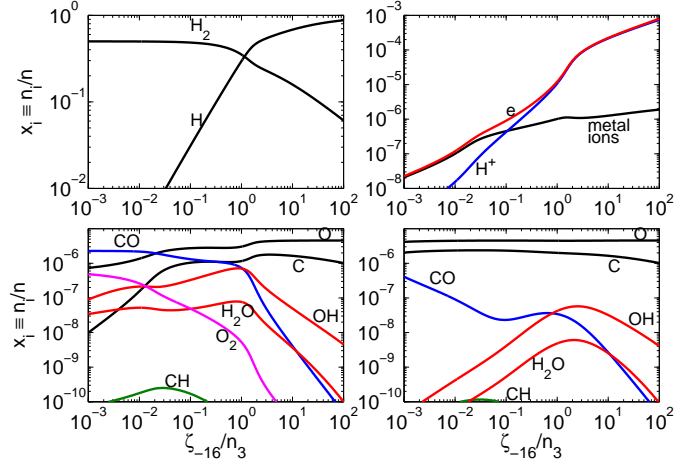


Figure 7. Fractional abundances ($x_i \equiv n_i/n$) as a function of ζ/n for $Z' = 10^{-2}$ and $T_2 = 1$. In the lower right panel $I_{\text{UV}}^0/n_3=1$, in all other panels $I_{\text{UV}}^0/n_3=0$.

and for our assumed $\zeta_{-16}/n_3=1$, CH is always removed by H atoms (reaction [R69]) rather than by metal species or protons. To a good approximation

$$x_{\text{CH}} = \frac{k_{\text{R56}} x_{\text{C}} x_{\text{H}_3^+} + k_{\text{R58}} x_{\text{C}} + x_{\text{H}_2}}{k_{\text{R69}} x_{\text{H}}}. \quad (40)$$

The numerator in this expression accounts for CH production initiated via the formation of CH₂⁺ by either radiative association (reaction [R58]) or proton transfer (reactions [R56]–[R57]) involving C or C⁺. The denominator accounts for removal by hydrogen atoms. As Z' is reduced and x_{H} increases, CH is rapidly removed, as seen in Figure 6. In general CH is a negligible hydride compared to OH or H₂O at low metallicity.

Finally, in the middle- and lower-right panels of Figure 6 we illustrate the effects of turning on a background FUV radiation field assuming $I_{\text{UV}}^0/n_3 = 1$. We solve Equations (8), and as Z' is reduced we vary the field intensity inside the parcels according to our dust-shielding formula Equation (10). Because we are assuming that the LW band is blocked for any Z' , the H and H₂ curves are unaffected when the FUV field is turned on. However, for $Z' \lesssim 0.1$ the OH, H₂O, and O₂ are removed by photodissociation as the dust opacity vanishes. CO is fully shielded by the blocked LW band and continues to be removed by He⁺ throughout. Nevertheless, the CO abundance is reduced when the FUV is turned on because of the suppression of the OH intermediary. Importantly, because the CO removal rate is not altered, the OH/CO abundance *ratio* is unaffected when the FUV is turned on, and the transition from the CO-dominated to the OH-dominated regimes still occurs near the H-to-H₂ transition. We discuss OH/CO further in §5.3.

5.2 Dependence on ζ/n for fixed Z'

We now consider the behavior as a function of ζ_{-16}/n_3 , for two values of Z' . In Figure 7, $Z' = 10^{-2}$ and ζ_{-16}/n_3 ranges from 10^{-3} to 10^2 . In Figure 8, $Z' = 1$ and ζ_{-16}/n_3 ranges from 10^{-2} to 10^3 . Our results for $Z' = 1$ are similar to those found by Lepp & Dalgarno (1996) in their study of X-ray driven chemistry at solar metallicity, where ζ is the X-ray ionization rate (see their Figures 1 and 2). See also Bayet et al. (2011), their Figure 3.

As seen in Figures 7 and 8, when ζ/n is small H₂ destruction

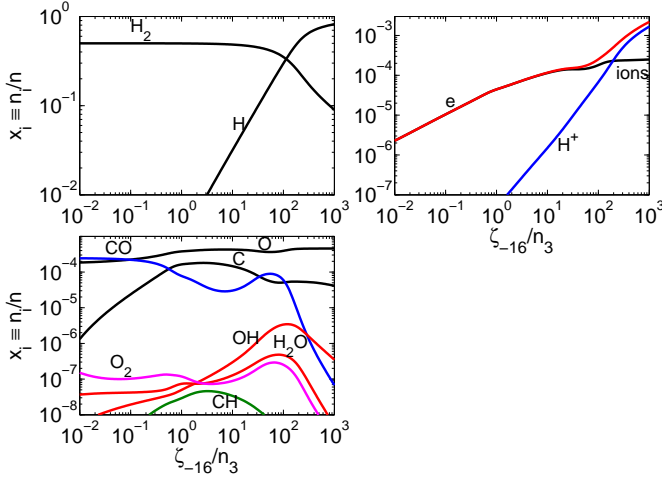


Figure 8. Fractional abundances ($x_i \equiv n_i/n$) as a function of ζ/n for $Z' = 1$, $T_2 = 1$, and $I_{UV}^0/n_3 = 0$.

by crx-ionization is ineffective and the hydrogen is fully molecular (upper-left panels of Figures 7 and 8). The H/H_2 ratio increases with ζ/n , and for $Z' = 10^{-2}$, the H-to- H_2 transition occurs at $\zeta_{-16}/n_3 \approx 1$. For $Z' = 1$ it occurs at $\zeta_{-16}/n_3 \approx 10^2$. This behavior is consistent with our Equation (23) for the location of the H-to- H_2 transition (for $\beta=1$).

The ionization fraction x_e is shown in the upper-right panels. It also increases with ζ/n . For example, for $Z' = 1$, x_e ranges from 2×10^{-6} to 2×10^{-4} for ζ_{-16}/n_3 ranging from 10^{-2} to 10^2 (see also Lepp & Dalgarno 1996, their Figure 1). At low ζ/n , and in the H_2 regime, the positive charge is carried by metals. This includes molecular ions, e.g., H_3^+ , HCO^+ , H_3O^+ , in addition to the atomic ions. At high ζ/n , and in the atomic regime, the positive charge is carried by protons, and $x_e \simeq x_{H^+}$.

The lower-left panels in Figures 7 and 8 show the C, O, OH, H_2O , O_2 , CH, and CO abundance fractions x_i . The steepening rise of x_{OH} toward the H-to- H_2 transition point and then the decline with ζ/n , is consistent with our approximate OH abundance scaling Equations (35) and (37). For example, for $Z'=1$, and for ζ_{-16}/n_3 between ~ 1 and 10^2 , x_{OH} increases linearly with ζ/n as given by Equation (35) for small x_O/x_e . For $\zeta_{-16}/n_3 \lesssim 1$, the oxygen to electron ratio becomes large and the variation of x_{OH} with ζ/n is moderated. For $\zeta_{-16}/n_3 \gtrsim 10^2$ the hydrogen becomes atomic and x_{OH} then decreases with the ionization rate and varies approximately as $(\zeta/n)^{-1}$ as given by Equation (37).

Similar behavior was found by Bayet et al. (2011) in their study of molecular chemistry at high cosmic-ray ionization rates (for models with fixed gas density). Their numerical results also show an OH abundance peak close to the H-to- H_2 transition point, but they did not discuss this connection.

At low ζ/n , and in the molecular regime, O_2 becomes abundant compared to OH, but as ζ/n increases the O_2/OH ratio decreases. Correspondingly, at low ζ/n in the H_2 regime, most of gas-phase carbon is locked in CO, and the C/CO ratio is small. The free atomic carbon increases with ζ/n and C/CO reaches a local maximum just before the H-to- H_2 transition point, and the subsequent sharp drop in the CO abundance. The slight rise in the CO abundance near the H-to- H_2 transition in Figure 8, is due to the OH maximum and the resulting enhanced CO production rate at this point.

The lower right panel of Figure 7 shows the effect of FUV

radiation, for our assumed $Z' = 0.01$ models for $I_{UV}^0/n_3 = 1$. Photodissociation suppresses the OH, H_2O and O_2 . At high ζ/n , and well inside the atomic regime, H^+ dominates the OH removal and the abundance curve is unaffected by photodissociation. Similarly H_2O and CH are suppressed by photodissociation when ζ/n is not too large. CO is shielded but is indirectly reduced by the photodissociation of the OH intermediary.

For $Z' = 1$ (Figure 8), dust-shielding is operative for all wavelengths, so that the photoprocesses are ineffective for all ζ/n , and we do not include an FUV panel for this model sequence.

5.3 Abundance Ratios: OH/ O_2 , C/CO and OH/CO

The C/CO, OH/ O_2 , and OH/CO abundance ratios are of particular interest. We plot them in Figure 9, as functions of Z' for $\zeta_{-16}/n_3 = 1$, and as functions of ζ_{-16}/n_3 for $Z' = 10^{-2}$, given our results presented in Figures 6 - 8. The solid curves are for FUV off, and the dashed curves are for FUV on with $I_{UV}/n_3 = 1$. The vertical dashed lines in Figure 9 indicate the positions of the H-to- H_2 transitions. For fixed $\zeta_{-16}/n_3 = 1$ the H-to- H_2 transition occurs at $Z' \approx 10^{-2}$, and the gas is atomic (molecular) to the left (right) of the dashed line. For fixed $Z' = 0.01$, the transition occurs at $\zeta_{-16}/n_3 \approx 1$, and the gas is atomic (molecular) to the right (left) of the dashed line. We consider the behavior of the C/CO, OH/ O_2 , and OH/CO abundance ratios in both the molecular and atomic regimes.

We begin with a discussion of C/CO and OH/ O_2 . These ratios are coupled in an important way in the molecular regime (Le Bourlot et al. 1993; Boger & Sternberg 2006; Wakelam et al. 2006). To see this we first write

$$\frac{x_{OH}}{x_{O_2}} \propto \left(\frac{\zeta_{-16}}{n_3} \right) \frac{1}{Z'} . \quad (41)$$

This follows because the O_2 formation rate is proportional to the atomic oxygen abundance which is proportional to Z' , and because the O_2 removal rate (via reactions [R49]-[R53]) is approximately proportional ζ/n . Alternatively, this is just the first-order scaling for x_{OH} with x_{O_2} approximately constant. Equation (41) accounts for the fact that OH/ O_2 can be large or small depending on Z' and ζ_{-16}/n_3 as seen in Figure 9 (and Figures 6 - 8).

As discussed in §2.3 there are two primary CO formation pathways, involving either OH as the main intermediary, via reactions [R70]-[R71] with C and C^+ , or involving O_2 via [R49]-[R51], again with C and C^+ . In general $C^+/C \ll 1$ in the molecular regime, but CO formation via C^+ can still contribute due to the large rate coefficients of the ion-molecule reactions. The C/CO ratio can now be understood qualitatively by considering a simplified formation-destruction equation for the CO,

$$\begin{aligned} (k_{OH}x_{OH} + k_{O_2}x_{O_2})x_C &= k_{R19}x_{He^+}x_{CO} \\ &= 0.5 \left(\frac{\zeta_{-16}}{n_3} \right) x_{He^+} . \end{aligned} \quad (42)$$

The left-hand side of this expression encapsulates CO formation, where $k_{OH} \equiv 10^{-9} \text{ cm}^3 \text{ s}^{-1}$ is the effective total rate coefficient for formation via OH (involving both C and C^+), and $k_{O_2} \equiv 3 \times 10^{-10} \text{ cm}^3 \text{ s}^{-1}$ is the effective rate coefficient for formation via O_2 . We assume that C^+/C is small so that the abundance of carbon species not locked in CO is represented by just the free atomic carbon abundance x_C . The middle term of Equation (42) is the CO destruction rate via dissociative charge transfer with He^+ (reaction [R19]). So long as this is also the dominant He^+ neutralization process, the rate equals the helium ionization rate on the

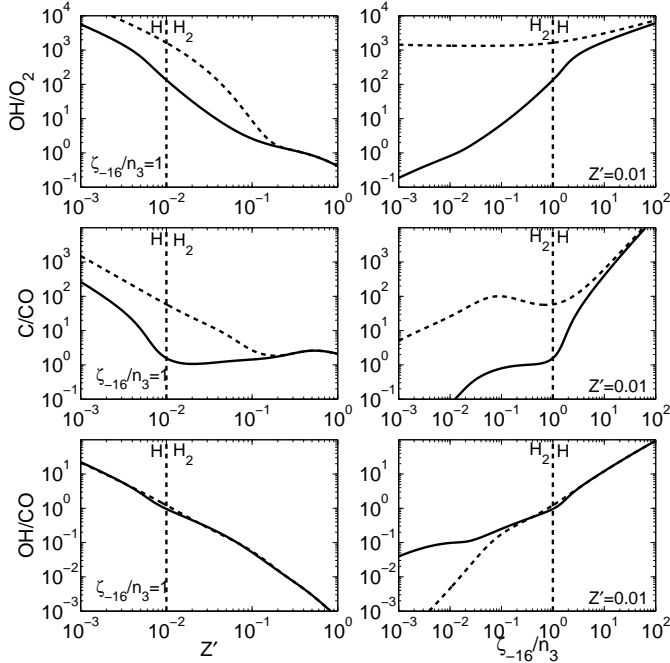


Figure 9. OH/O₂, C/CO, and OH/CO abundance ratios as a function of Z' for fixed $\zeta_{-16}/n_3 = 1$ (left) and as a function of ζ/n for fixed $Z' = 10^{-2}$ (right). In both panels we assume $T_2 = 1$ and $I_{UV}^0/n_3 = 0$ (solid line) and $I_{UV}^0/n_3 = 1$ (dashed line).

right hand side. Because the helium is predominantly neutral we set $x_{He} = A_{He} = 0.1$.

At high ζ/n and/or low Z' (but still in the molecular regime), OH/O₂ becomes large, according to Equation (41), and we then have

$$x_C \simeq \frac{0.5}{k_{OH}x_{OH}} \left(\frac{\zeta}{n} \right) A_{He} \simeq 0.4 A_C Z' . \quad (43)$$

Here we use our first order expression for the OH abundance in the molecular regime

$$x_{OH} \simeq 4 \times 10^{-8} \left(\frac{\zeta_{-16}}{n_3} \right) \frac{1}{Z'} . \quad (44)$$

The prefactor of 4×10^{-8} is obtained from our numerical calculations for $\zeta_{-16}/n_3 = 1$ and $Z' = 1$ (see Figure 6). Importantly, Equation (43) shows that when OH/O₂ $\gg 1$, x_C is independent of the ionization parameter ζ/n . Furthermore, x_C approaches saturation and becomes comparable to the total carbon abundance $A_C Z'$. In this limit the analysis shows that C/CO becomes large, but numerically we find that it remains of order unity in the H₂ regime.

When OH/O₂ $\ll 1$, as occurs at low ζ/n and/or high Z' (again in the molecular regime) we have

$$x_C = \frac{0.5}{k_{O_2}x_{O_2}} \left(\frac{\zeta}{n} \right) A_{He} \simeq 10^{-6} \left(\frac{\zeta_{-16}}{n_3} \right) \ll A_C Z' . \quad (45)$$

Here we have assumed $x_{O_2} \simeq 10^{-7}$, and to first-order independent of Z' and ζ/n (as found for the HIP in our full 2D computations in §6). In this limit the free atomic carbon abundance is proportional to ζ/n , but C/CO remains small.

The above discussion for OH/O₂ and C/CO is for the H₂ regime. In the atomic regime, x_{OH} and x_{O_2} are given by Equations

(37) and (39), and

$$\frac{x_{OH}}{x_{O_2}} \simeq 6.7 \left(\frac{\zeta_{-16}}{n_3} \right)^{1/2} \frac{1}{Z'} . \quad (46)$$

As Z' becomes small OH/O₂ $\gg 1$, as expected.

In the atomic regime, the CO is formed mainly via the C+OH channel, and continues to be removed by He⁺. Crucially however, the He⁺ is no longer removed by CO but by charge transfer with atomic and molecular hydrogen, so that

$$x_{He^+} = \frac{0.5}{(k_{R21} + k_{R22})x_{H_2} + k_{R20}x_H} \left(\frac{\zeta}{n} \right) A_{He} , \quad (47)$$

independent of Z' . In this limit

$$\frac{x_C}{x_{CO}} = \frac{k_{R19}x_{He^+}}{k_{R70}x_{OH}} \simeq 0.5 \left(\frac{\zeta_{-16}}{n_3} \right)^{1.5} \frac{1}{Z'} , \quad (48)$$

and C/CO grows without limit. As indicated by Equations (46) and (48), in the atomic regime the OH/O₂ and C/CO ratios are decoupled.

We now consider OH/CO. Well inside the molecular regime where a large fraction of the carbon is locked in CO, the OH/CO ratio is small. In the atomic regime OH/CO $\gg 1$. In general the transition from the “OH-dominated” to “CO-dominated” regimes occurs close to the H-to-H₂ transition point. This is seen in Figure 9. We can write down approximate expressions for x_{OH}/x_{CO} as follows. At high Z' , and assuming most of the carbon is locked in CO, $x_{CO} \propto Z'$ so that

$$\frac{x_{OH}}{x_{CO}} \propto \frac{1}{Z'} x_{OH} \propto \frac{\zeta}{n} \left[1 + 0.27 \frac{x_O}{x_e} \right] \frac{1}{Z'^2} , \quad (49)$$

where here we have used Equation (35) for x_{OH} . In this limit OH/CO varies as $1/Z'^2$, and sublinearly with ζ/n .

In the atomic regime CO is formed via the OH+C channel, and is still removed by He⁺, so that

$$\frac{x_{OH}}{x_{CO}} = \frac{k_{R19}x_{He^+}}{k_{R70}x_C} \simeq 10^{-2} \left(\frac{\zeta_{-16}}{n_3} \right) \frac{1}{Z'} , \quad (50)$$

where $x_C = A_C Z'$, and x_{He^+} is given by Equation (47). Once again, because OH contains one heavy element and CO consists of two, OH/CO varies as $1/Z'$ in the low Z' limit. The linear dependence on ζ/n enters via x_{He^+} as given by Equation (47).

The dashed curves in Figure 9 are for FUV on with $I_{UV}^0/n_3 = 1$. The OH/O₂ ratio is now inversely proportional to the O₂ photodestruction rate and is independent of ζ/n , but the dependence on Z' is unaffected. C/CO is enhanced due to the indirect reduction of CO via photodissociation of the OH and the O₂. Importantly, so long as CO is mainly formed via the OH intermediary, OH/CO is unaffected by photodissociation of the OH. This is seen in the lower panels of Figure 9, in which the dashed (FUV on) and solid (FUV off) curves coincide. The OH/CO curves do diverge for very low ζ/n at fixed Z' , because when FUV is on the OH (and O₂) abundances become so small that residual processes start contributing to the CO production. However in the (atomic) “OH-dominated” regime photodissociation of the OH never affects the OH/CO ratio. In particular, photodissociation does not affect the transition points from the CO-dominated to OH-dominated regimes.

6 CHEMICAL ABUNDANCES FOR Z' VERSUS ζ/n

Given our description in §4 and 5 of the basic chemical behavior and regimes, we now present computations that span our full two-

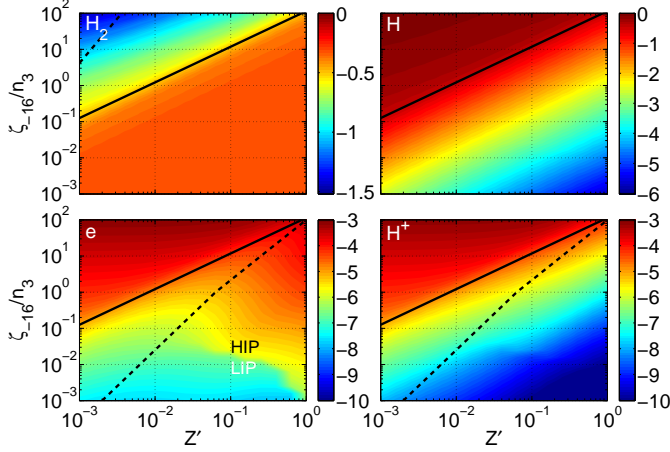


Figure 10. Fractional abundances in the Z' versus ζ_{-16}/n_3 plane, for $I_{UV} = 0$ and $T_2 = 1$. (a) Upper left panel shows $\log x_{H_2}$, ranging from -1.5 to 0. The solid line is the H-to- H_2 transition where $x_{H_2} = x_H$ (shown in all panels), and the dashed line is where gas phase and dust grain H_2 formation rates equal. (b) Upper right panel is $\log x_H$, from -6 to 0. (c) Lower left panel is $\log x_e$, from -10 to -3. The abrupt switch from HIP to LIP is indicated. (d) Lower right panel is $\log x_{H^+}$, from -10 to -3, the dark blue area indicates values lower than the color-bar range. In both lower panels, the dashed curves are where $x_{H^+} = 0.25x_e$.

dimensional (2D) Z' versus ζ/n parameter space. For our 2D computations we vary Z' from 10^{-3} to 1 and ζ_{-16}/n_3 from 10^{-3} to 10^2 . We again assume that the grain H_2 formation rate coefficient varies linearly with Z' ($\beta = 1$ in Equation [1]), and we show results for FUV off (§6.1 and 6.2) and on (§6.3), according to Equations (3)-(6), and (8)-(10). We again assume $T_2 = 1$ gas. We present the atomic and molecular abundances in the Z' versus ζ_{-16}/n_3 plane as color-contour plots, in which the color varies with $\log x_i$, from large (red) to small (blue). The displayed dynamic-ranges for the $\log x_i$ differ for different species i , and are indicated for each panel.

6.1 H, H_2 , H^+ , and e

In Figure 10 we show the atomic and molecular hydrogen fractions x_H and x_{H_2} , and the electron and proton fractions, x_e and x_{H^+} , in the Z' versus ζ_{-16}/n_3 plane assuming FUV off ($I_{UV}^0 = 0$), as given by the solutions to Equations (3)-(6).

The upper left panel shows x_{H_2} for the range $10^{-1.5}$ to 1. The upper right panel shows x_H from 10^{-6} to 1. The solid diagonal line shows the H-to- H_2 transition where $x_H = x_{H_2}$. Its slope, $(\zeta/n) \propto Z'$, and position is consistent with our Equation (23). We draw the H-to- H_2 transition line in all of our parameter-space plots to delineate the atomic and molecular hydrogen regimes. As seen in Figure 10, the gas becomes atomic at a given Z' for sufficiently large ζ/n , or at sufficiently low Z' for a given ζ/n . In the panel for x_{H_2} , we also draw a dashed line where the H_2 formation rates in the gas-phase and on grains are equal. The position of this line is in good agreement with our Equation (26) for $\beta = 1$. Grain H_2 formation is dominant in most of our parameter space including in the atomic regime, except in the upper-left corner where Z' is very low and ζ_{-16}/n_3 is large.

The lower left and right panels of Figure 10 shows x_e and H^+ ranging from 10^{-10} to 10^{-3} . Several zones may be identified for the fractional ionization x_e . The solid line again divides the

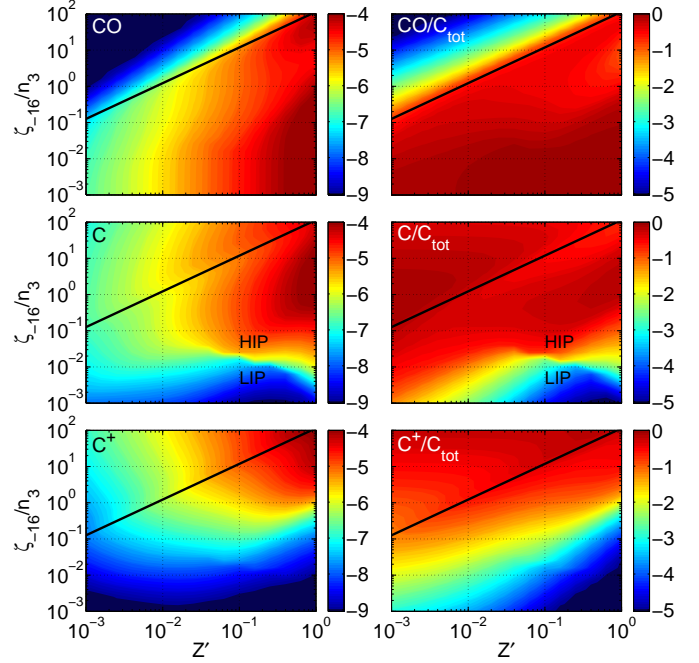


Figure 11. CO, C, and C^+ in the Z' , ζ_{-16}/n_3 plane with $T_2 = 1$ and $I_{UV}^0 = 0$. The left panels show logarithmic abundances relative to total hydrogen density, $\log x_{CO}$, $\log x_C$ and $\log x_{C^+}$ ranging from -9 to -4. The right panels show the log abundances relative to the total elemental carbon ($C_{tot} \equiv 2.9 \times 10^{-4} Z'$), ranging from -5 to 0. The dark blue (red) areas indicate values lower (higher) than the color-bar range. The H-to- H_2 transition is at the solid line. The LIP and HIP zones are indicated.

parameter-space into the atomic and molecular regimes. The abrupt switch from LIP to HIP conditions can be seen at $\zeta_{-16}/n_3 \approx 10^{-2}$ to 10^{-3} . The dashed curve is where $x_{H^+} = 0.25x_e$. To the left of this curve H^+ becomes the dominant positive charge carrier, and in the atomic regime x_e varies as $(\zeta_{-16}/n_3)^{1/2}$ (see Equation [18]). To the right of the dashed curve metals dominate the fractional ionization. Thus, for a given ζ_{-16}/n_3 , x_e is maximal at very low Z' , and decreases across the H-to- H_2 transition as x_{H^+} drops. The electron fraction then increases again across the dashed curve, as the metals take over. This is the behavior seen for x_e versus Z' in our fiducial 1D cut shown in Figure 6 for $\zeta_{-16}/n_3 = 1$. At fixed Z' , x_e increases monotonically with ζ/n , as we have also seen in Figures 7 and 8.

6.2 CO, C, C^+ , OH, H_2O and O_2

Our 2D results for the C, CO, OH, H_2O and O_2 abundances, with FUV off, are shown in Figures 11 and 12. In the left hand panels we show the x_i . In the right hand panels we normalize to the total carbon or oxygen abundances, $C_{tot} = A_C Z'$ and $O_{tot} = A_O Z'$. In Figure 11 we show CO/C_{tot} , C/C_{tot} and C^+/C_{tot} , and in Figure 12 we show OH/O_{tot} , H_2O/O_{tot} , and O_2/O_{tot} .

The upper panels of Figure 11 display the CO abundances, with x_{CO} ranging from 10^{-4} to $\sim 10^{-7}$ in the molecular regime (below the solid line) and down to less than 10^{-9} in the atomic regime. These plots show that in the H_2 regime a large fraction, 30-100 %, of the available carbon is always locked in CO. This is true even at very low Z' , so long as ζ/n is small enough for the hydrogen to be molecular. The general result is that gas-phase CO formation is efficient at all metallicities so long as the hydrogen is molec-

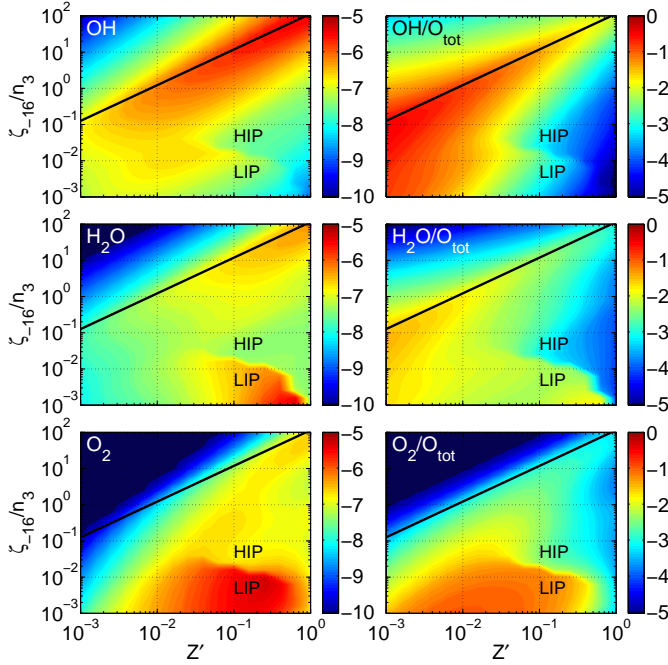


Figure 12. OH, H₂O, and O₂ in the Z' , ζ_{-16}/n_3 plane with $T_2 = 1$ and $I_{UV}^0 = 0$. The left panels show logarithmic abundances relative to total hydrogen density, $\log x_{OH}$, $\log x_{H_2O}$ and $\log x_{O_2}$, ranging from -10 to -5. The right panels show the log abundances relative to the total elemental oxygen ($O_{tot} \equiv 4.9 \times 10^{-4} Z'$), ranging from -5 to 0. The dark blue (red) areas indicate values lower (higher) than the color-bar range. The H-to-H₂ transition is at the solid line. The LIP and HIP zones are indicated.

ular. Thus, in the H₂ regime x_{CO} varies approximately linearly with Z' and very weakly with ζ/n . However, in the atomic regime x_{CO} drops very sharply with decreasing Z' or increasing ζ/n , and CO becomes a trace species. In this regime $x_{CO} \propto (\zeta/n)^{-1.5} Z'^2$ as seen in Figure 11 and consistent with Equation (48).

The middle and lower panels of Figure 11 show the free atomic and ionized carbon abundances. Even in the H₂ regime, a significant fraction ($\sim 50\%$) of the carbon remains atomic as long as ζ/n is not too low, especially in the HIP. But at sufficiently low ζ/n for any Z' the atomic carbon vanishes and is fully absorbed into CO. This is the behavior we discussed in §5.3. In the atomic regime where CO vanishes most of the carbon remains atomic as long as the ionization parameter is not too large, with $C^+/C < 1$ for $\zeta_{-16}/n_3 \lesssim 50$. For higher ionization parameters most of the carbon is ionized.

The upper panels of Figure 12 show the behavior for OH. To first order, $x_{OH} \propto (\zeta/n)/Z'$ in the molecular regime (see Equation [35]) and the color contours for x_{OH} run approximately parallel to the H-to-H₂ transition line. As we have discussed, for any Z' we expect the OH abundance to be maximal near the H-to-H₂ transition. This is indeed seen in Figure 12. Along the transition line, x_{OH} ranges from $\approx 3 \times 10^{-6}$ at $Z' = 1$ to $\approx 10^{-7}$ at $Z' = 10^{-3}$. The reduction of x_{OH} along the transition line is due to H⁺ removal of the OH (reaction [R43]) in addition to removal by atomic oxygen and other metals. Along the transition line the OH is formed mainly via the charge-transfer route with H⁺ (reaction [R14]). Well within the molecular regime where H⁺ becomes small the H₃⁺ proton transfer route predominates (reaction [R28]). The jump in x_{OH} at the HIP-to-LIP boundary is due, in part, to the sudden change in the H₃⁺ abundance at the phase

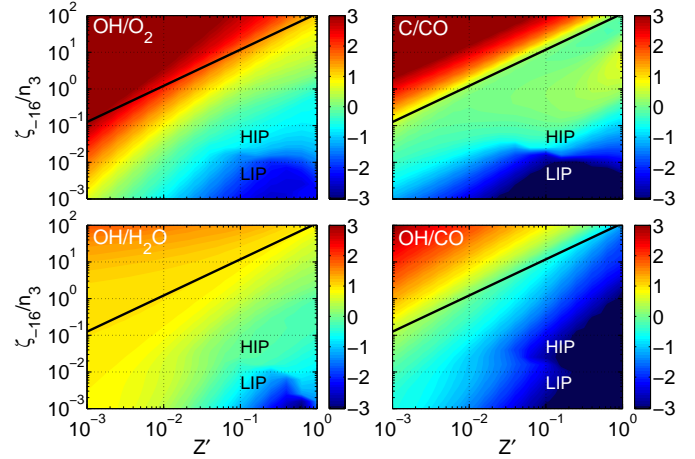


Figure 13. log of the abundance ratios, OH/O₂, C/CO, OH/H₂O and OH/CO in the Z' , ζ_{-16}/n_3 plane ranging from -3 to 3, for $T_2 = 1$ and $I_{UV}^0 = 0$. The dark blue (red) areas indicate values lower (higher) than the color-bar range. The H-to-H₂ transition is at the solid line. The LIP and HIP zones are indicated.

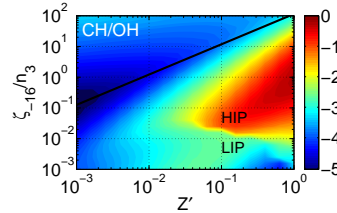


Figure 14. log of the CH/OH abundance ratio in the Z' , ζ_{-16}/n_3 plane, ranging from -5 to 0, for $T_2 = 1$ and $I_{UV}^0 = 0$. The dark blue (red) areas indicate values lower (higher) than the color-bar range. The H-to-H₂ transition is at the solid line.

transition. In the atomic regime the OH abundance decreases, and $x_{OH} \propto (\zeta/n)^{-1} Z'$ (see Equation [37]), but the relative fraction OH/O_{tot} is relatively large in this regime, as seen in the upper-right panel.

The middle panels of Figure 12 show that x_{H_2O} is weakly dependent on Z' and ζ/n in the H₂ regime. We find $x_{H_2O} \approx 10^{-8}$ to 10^{-7} in the HIP and $\sim 3 \times 10^{-6}$ in the LIP. In the atomic regime the H₂O abundance decreases, and $x_{H_2O} \propto (\zeta/n)^{-1} Z'$ (see Equation [38]).

The lower panels of Figure 12 show that as expected x_{O_2} is also weakly dependent on Z' and ζ/n in much of the H₂ regime. In the HIP $x_{O_2} \approx 2 \times 10^{-7}$ is a characteristic value. For the LIP $x_{O_2} \approx 2 \times 10^{-6}$. At sufficiently low Z' removal of the O₂ by H⁺ rather than metals takes over, and x_{O_2} drops. In the atomic regime the O₂ rapidly vanishes as $(\zeta/n)^{-1.5} Z'^2$ (see Equation [39]).

Figure 13 shows the abundance ratios for OH/O₂, C/CO, OH/H₂O, and OH/CO, in our Z' versus ζ/n parameter space. In these plots we limit the dynamic ranges of the displayed ratios from 10^{-3} to 10^3 .

Most of the variation in OH/O₂ is due to the variation in x_{OH} . At low ζ/n and/or at high Z' , in the molecular regime, OH/O₂ becomes small (see Equation [41]). Still in the molecular regime, OH/O₂ approaches unity as Z' is decreased or as ζ/n is increased. For example, OH/O₂ ≈ 1 at $Z' = 3 \times 10^{-3}$ for $\zeta_{-16}/n_3 = 10^{-3}$ or at $Z' = 1$ for $\zeta_{-16}/n_3 = 20$. At still lower Z' , or higher ζ/n , OH begins to dominate over O₂. In the atomic regime OH *always*

strongly exceeds O_2 as it must, due to the Z' versus Z'^2 metallicity scalings for the OH and O_2 abundances in the low Z' limit.

As discussed in §5.3, the C/CO and OH/ O_2 abundance ratios are strongly coupled in the molecular regime. So long as OH/ O_2 is not too low C/CO remains of order unity. At very low ζ/n , OH/ O_2 becomes small and consequently C/CO strongly decreases (approximately as ζ/n) as all of the carbon is driven to CO. For example, at solar metallicity, $C/CO \approx 0.1$ for $\zeta_{-16}/n_3 = 10^{-1}$, but $C/CO \approx 6 \times 10^{-3}$ for $\zeta_{-16}/n_3 = 10^{-2}$. In the atomic regime, C/CO rapidly increases as the CO vanishes.

The lower-left panel of Figure 13 shows OH/ H_2O . In the atomic regime OH/ $H_2O \sim 10$ and is approximately constant, as set by the branching ratios of H_3O^+ dissociative recombination, and the preferential removal of H_2O by protons. In the molecular regime, OH/ H_2O varies and can become small as x_{OH} decreases more rapidly at high Z' and low ζ/n .

The OH/CO ratio for ζ/n versus Z' is shown in the lower-right panel of Figure 13. As expected, OH/CO $\ll 1$ well inside the H_2 regime. In the atomic regime OH/CO $\gg 1$. The switch from the OH- to CO-dominated regimes occurs close to the H-to- H_2 transition line.

Finally in Figure 14 we show the CH/OH abundance ratio within our Z' versus ζ/n parameter space. The CH/OH ratio approaches unity at high Z' within the HIP. As expected, CH vanishes and CH/OH becomes small at low Z' and into the atomic regime. OH is the dominant heavy molecule at low Z' and/or high ζ/n .

6.3 FUV on

In Figures 15, 16 and 17, we show 2D model results for FUV on. We again assume $I_{UV}^0/n_3 = 1$, and vary I_{UV} inside the parcels according to our dust shielding formula (Equation [10]). As before, we assume that the LW band is always completely blocked so that the H_2 and CO are shielded from direct photodissociation at all Z' . However OH, H_2O , and O_2 are photodissociated when Z' is small and the dust shielding vanishes. For our assumed $I_{UV}^0/n_3 = 1$ photodissociation dominates over chemical removal for $Z' \lesssim 0.1$ for the HIP, and for $Z' \lesssim 0.4$ for the LIP.

Figure 15 shows the OH, H_2O , and O_2 abundances with FUV on. For $\zeta_{-16}/n_3 \gtrsim 1$, chemical removal remains dominant at all Z' . For lower ionization parameters, photodissociation becomes rapid once the parcels become unshielded at $Z' \lesssim 0.1$, and OH, H_2O , and O_2 abundances are reduced. Reduction of O_2 by FUV is especially effective because (a) the OH intermediary required for O_2 formation is removed and (b) the O_2 is itself directly photodissociated.

The upper panel of Figure 16 shows that the CO vanishes within the H_2 regime as the OH (and O_2) are photodissociated, even though the CO itself is fully shielded. CO then becomes a trace species as Z' is reduced, and most of the carbon remains atomic or ionized as shown in the middle panels.

Figure 17 shows the OH/ O_2 , C/CO, OH/ H_2O , and OH/CO abundance ratios for the computations with FUV on. The OH/ O_2 ratio becomes very high in most of the parameter space. When photodissociation is effective we find OH/ $H_2O \approx 10$, now also in the H_2 regime, not just in the atomic regime. This is now due to preferential formation of OH in the dissociative recombination of H_3O^+ , and the higher H_2O photodissociation rate compared to OH. Once photodissociation becomes effective the OH/ O_2 and C/CO ratios decouple, and the C/CO ratio becomes large as the CO vanishes.

Importantly, the OH/CO ratio is unaffected by the FUV, because only the OH, that is required for the formation of the CO,

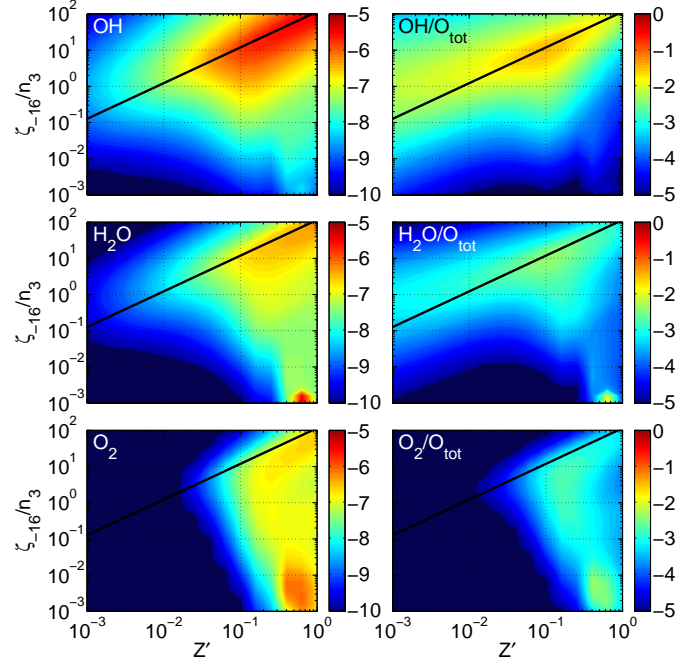


Figure 15. The same as Figure 12 but with $I_{UV}^0/n_3 = 1$.

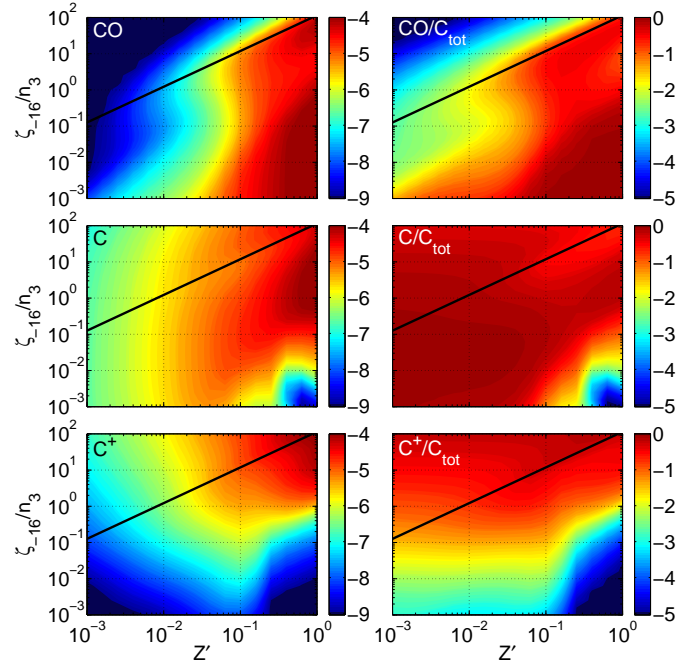


Figure 16. The same as Figure 11 but with $I_{UV}^0/n_3 = 1$.

is reduced by the FUV. Thus the transition from the CO to OH dominated regimes still occurs close to the H-to- H_2 transition line (as given by Equation [23]), whether or not FUV is off or on. Inevitably, OH becomes the dominant heavy molecule in the limit of low metallicity.

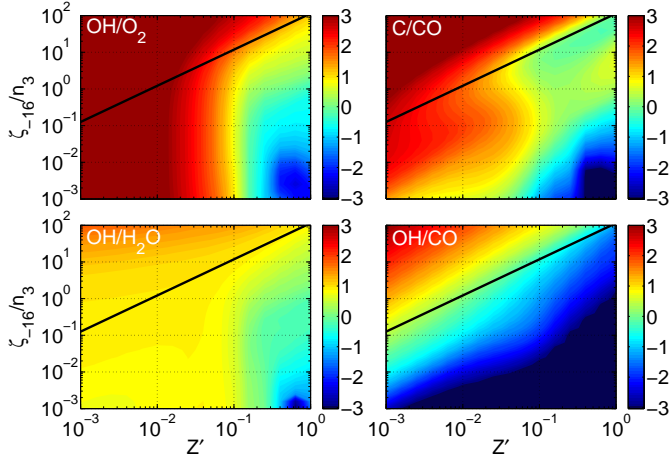


Figure 17. The same as Figure 13 but with $I_{UV}^0/n_3 = 1$.

7 COMPARISON TO TIME-DEPENDENT MOLECULE FORMATION SEQUENCES

Before concluding it is of interest to compare our results assuming equilibrium ionization-driven chemistry for the the bulk “dense-cold-ISM”, to the time-dependent calculations presented by Omukai et al. (2005) in their study of collapsing clouds at low metallicities. As we noted in §1, in the collapsing cloud calculations the chemistry consists of intrinsically time-dependent reformation sequences, and is not ionization-driven as in our study. Because ionization (and/or photodissociation) by external driving sources is not included in the collapsing cloud computations, these systems can never formally reach a formation-destruction equilibrium. Nevertheless, some qualitative comparisons can be made.

For this purpose we consider the Omukai et al. abundance versus density curves (their Figs. 5 and 12) for H and H₂, for C⁺, C, and CO, and for O, OH, and H₂O. (They do not display results for CH and other carbon hydrides.) In their scheme the gas density, $n(t)$, increases with time t and the non-equilibrium chemical abundances vary with gas density, which is a proxy for time. Omukai et al. display the chemical abundances as functions of density, but the times associated with each density and chemical state are not shown. The precise behavior depends on initial conditions and the varying temperatures as set by compressive heating and radiative cooling. For a very wide range of gas densities (10^2 to 10^8 cm⁻³) and metallicities (down to $Z' \sim 10^{-3}$) the gas temperature is in our cold gas ($T \sim 100$ K) regime, and the chemistry is dominated by the two-body reactions.

The time-dependent curves show that the atomic to molecular hydrogen conversion points occur at larger densities for lower metallicities, as is expected given their ($\beta = 1$) assumption that the H₂ grain formation time scale varies inversely with Z' . They also find that once the hydrogen is fully molecular, the conversion to CO is always complete. This is qualitatively similar to our finding that CO production is efficient in the H₂ regime. However, in the reformation sequences, conversion to CO occurs before the H/H₂ transition, and CO exists within part of the atomic regime. This probably reflects the fact that He⁺ has recombined and the CO removal rates have become vanishingly small (with photodissociation also excluded). For our ionization-driven chemistry we find that CO always disappears close to the H/H₂ transition point as set by the ionization parameter ζ/n (as opposed to a time-dependent density

n). Furthermore, in our models CO is not always fully formed even within the H₂ regime.

Second, in the contracting clouds OH/CO $\ll 1$ in the H₂ regime. However, it is unclear how the OH/CO ratio would be affected by steady background ionization⁷, which also enables a well-defined reference equilibrium state for any density and temperature. In the (early time) atomic regimes, OH/CO is large, although not as large as given by our OH/CO $\sim 1/Z'$ scaling rule. As we have demonstrated mathematically, this rule must hold for low- Z' ionization-driven sequences in the atomic regime.

Omukai et al. also find that OH/H₂O > 1 in the cold-gas regime as is expected for OH and H₂O formation via dissociative recombination. They did not present results for other hydrides, in particular CH, which could in principle compete with OH. However, as we have shown, at low Z' into the atomic regime, CH vanishes compared to OH even for comparable carbon and oxygen elemental abundances.

Our study of ionization-driven molecular equilibrium states down to low metallicity is complementary to the time-dependent molecular formation sequences in collapsing clouds. An analysis of low-metallicity time-dependent formation chemistry with the inclusion of background irradiation and ionization would be valuable, and will be presented in forthcoming papers.

8 SUMMARY AND DISCUSSION

In this paper we have presented a numerical and analytic study of interstellar gas-phase ion-molecule chemistry in cold dense gas, from solar metallicity Galactic conditions into the domain of interstellar media at very low metallicities, and related properties at high ionization rates. Relevant astrophysical environments include the cool ISM in low metallicity dwarf galaxies, early enriched clouds at reionization and the Pop-II star formation epoch, and in dense gas exposed to intense X-ray or cosmic-ray sources. We consider a wide range of overall heavy-element abundances or metallicities, Z' , and cloud ionization parameters ζ/n . Here ζ is the total ionization rate, and n is the hydrogen gas volume density.

We have focused on the steady-state behavior and trends for H₂, CO, CH, OH, H₂O, and O₂, and the associated diagnostic abundance ratios CO/H₂, C/CO, OH/CO, and OH/O₂. In §2 we present a detailed discussion of the hydrogen-carbon-oxygen chemical networks and the varying molecule formation-destruction pathways, down to the low metallicity regime.

We have considered idealized shielded or partially shielded “one-zone” isothermal gas parcels, for which the steady-state abundances of the atomic and molecular species are fully determined by the assumed metallicity and ionization parameter, as discussed in §3. We adopt a gas temperature of 100 K appropriate for cooled gas at low metallicity. We imagine that the (hydrogen) ionization rate ζ is provided by penetrating cosmic-rays or X-rays, and the associated secondary electrons. When FUV photo(destruction) processes are included a third parameter enters, the ratio I_{UV}^0/n of the FUV intensity to the gas density. We have then considered two types of models. First are sequences for which irradiation by external FUV is fully excluded. Second are models for which FUV is turned on, but the H₂ Lyman-Werner photodissociation band remains fully blocked even when the parcels are optically thin

⁷ Omukai (2012) include background ionization in their revised cooling/fragmentation computations, but do not present results for the chemistry.

to longer wavelength radiation. Our overall parameter space is, $10^{-3} \leq Z' \leq 1$ and $10^{-3} \leq \zeta_{-16}/n_3 \leq 10^2$. We assume a solar relative abundance pattern for the heavy elements, with absolute total abundances proportional to Z' . For models with FUV-on we set $I_{UV}/n_3 = 1$. We adopt relative photorates appropriate for a diluted 10^5 K blackbody field as representative of pop-III star spectra. Our computed atomic and molecular photodissociation and photoionization rates for such spectra are presented in Table 2.

The H/H₂ balance is critical to the overall chemical behavior since the ion-molecule sequences for the metal-bearing species all require at least some H₂. In §4 we present general purpose analytic results for the H-to-H₂ transition points and H₂ fractional abundances for optically thick conditions (i.e. no LW photodissociation) in which the H₂ is destroyed by ionization (by cosmic-rays or X-rays) and is formed on dust-grains or in the gas phase via the H⁻ negative ion. We assume that the dust-to-gas ratio and H₂ grain formation efficiency vary as a simple power-law of the metallicity. The ionization parameters at the H-to-H₂ transition points in the limits of grain versus gas-phase H₂ formation are given by our Equations (21) and (23). The H₂ abundances (in the atomic regime) are given by Equations (29) and (31). We have verified our H/H₂ analysis with our detailed full chemistry computations in §5 and 6.

For our chemical study we have first considered 1D cuts, for varying Z' and fixed ζ/n , and second for varying ζ/n at fixed Z' , with and without FUV. These computations are presented in §5, and enable our development of abundance scaling formulae, mainly for OH, O₂ and CO, in both the molecular and atomic hydrogen regimes, from high to low metallicity. The division between these regimes in our full Z' versus ζ/n parameter space depends on how the dust-to-gas ratio varies with metallicity (§4). In our numerical calculations (§5 and 6) we have assumed a linear variation.

In §6 we present the results of our chemical computations as color-contour plots in our 2D, Z' versus ζ/n parameter space. Our primary results, all for steady state conditions, are as follows. First, in the absence of photodissociation CO molecules always form efficiently even at very low Z' provided ζ/n is small enough for the hydrogen to become molecular. (The time-scale for such conversion may be long at early cosmic times as we have estimated in §4.2.) The C/CO abundance ratio grows to ~ 1 at high ζ/n but not much larger, again so long as the conversion to H₂ is complete.

Second, we find that the OH abundances are maximal near the critical H-to-H₂ transition points. This is a very general trend also encapsulated in our analytic expressions for the OH abundance in the atomic and molecular regimes (Equations [35] and [37]). A large fraction of the available gas-phase oxygen is driven to OH at low Z' , and the OH persists within the atomic regime (e.g., Figure 12). To first-order, the OH abundance is proportional to ζ/n in the molecular regime, but inversely proportional to ζ/n in the atomic regime.

Third, the OH/CO abundance ratio approaches unity near the H-to-H₂ transition points, and increases without limit, as $1/Z'$, into the (low-metallicity) atomic regime. The behavior of the OH/CO ratio is not affected by FUV photodissociation of the OH so long as the CO is shielded by H₂.

Fourth, the O₂/OH ratio becomes large within the molecular regime at sufficiently low ζ/n and increasing metallicity. In the molecular regime C/CO and O₂/OH are anticorrelated. However, OH is always the dominant oxygen-bearing molecule at sufficiently low Z' . Furthermore, even for comparable carbon and oxygen elemental abundances, OH/CH $\gg 1$ at low metallicities, and OH becomes the dominant heavy-bearing molecule at low Z' .

Our study indicates that for ionization parameters character-

istic of the Milky Way and present-day galaxies, much of the cold dense low-metallicity ISM for the Pop-II generation would have been OH-dominated and atomic rather than CO-dominated and molecular. However, for sufficiently low ionization parameters conversion to H₂ will occur for FUV-shielded gas. Because the gas phase processes enable complete incorporation of carbon into CO even at very low metallicity, the CO abundance will remain linearly proportional to the overall metallicity and carbon abundance in this regime. Observationally, CO rotational line emissions then remain good proxy tracers for the H₂, but the emissions may become optically thin even for the dominant isotope, in which case the elemental carbon abundances affect the CO-to-H₂ conversion factors. For high metallicity systems for which the H₂ and CO formation times are shorter, conversion to CO may nevertheless not always be complete when the ionization parameters are large even for fully FUV-shielded H₂ gas. This is relevant for observations of galaxies with elevated star-formation and enhanced cosmic-ray ionization rates. For such systems, CO may not be a reliable tracer of the H₂ even in cosmic-ray or X-ray dominated cores (see also Bisbas et al. 2015). Detailed radiative transfer computations are required to estimate CO emission line brightness temperatures and associated CO-to-H₂ conversion factors in this regime.

As we have demonstrated in this paper, large OH abundances may persist in shielded atomic gas even at very low metallicities. This is of particular interest because observations of (radio-wave) “conjugate” OH rotational satellite lines may be used to probe or set limits on spatial and temporal variations of fundamental quantities such as the fine-structure-constant and/or the electron-to-proton mass ratio (e.g., Kanekar et al. 2004, 2012; Kozlov & Levshakov 2013). Observations of OH at high redshift, perhaps feasible given the large expected abundances, could provide a broad cosmological baseline for investigating such variations. Probes via CH, e.g. via the Λ -doublet transitions (de Nijs et al. 2012; Truppe et al. 2013) would be much less promising.

In future searches for molecules at the reionization epoch (e.g., Carilli 2011; Heywood et al. 2011; Lidz et al. 2011; Muñoz & Furlanetto 2013) OH may be a better target than CO.

ACKNOWLEDGMENTS

We thank Alex Dalgarno, Avi Loeb, Evelyne Roueff, and Ewine van Dishoeck for helpful conversations during the course of this work. We thank the referees for helpful comments that have improved our paper. S.B. acknowledges support from the Raymond and Beverly Sackler Tel Aviv University – Harvard Astronomy Program. This work was also supported in part by the DFG via German – Israeli Project Cooperation grant STE1869/1-1/GE625/15-1, and by a PBC Israel Science Foundation I-CORE Program grant 1829/12.

REFERENCES

- Asplund, M., Grevesse, N., Sauval, A. J., & Scott, P. 2009, *ARAA*, 47, 481
- Balakrishnan, N. 2004, *Geophys. Res. Lett.*, 31, L04106
- Bayet, E., Williams, D. A., Hartquist, T. W., & Viti, S. 2011, *MNRAS*, 414, 1583
- Beers, T. C., & Christlieb, N. 2005, *ARAA*, 43, 531
- Bisbas, T. G., Papadopoulos, P. P., & Viti, S. 2015, eprint ArXiv 1502.04198

- Black, J. H., & Dalgarno, A. 1973, *ApJ*, 184, L101
- Boger, G. I., & Sternberg, A. 2005, *ApJ*, 632, 302
- . 2006, *ApJ*, 645, 314
- Bolatto, A. D., Wolfire, M., & Leroy, A. K. 2013, *ARAA*, 51, 207
- Bovino, S., Grassi, T., Schleicher, D. R. G., & Latif, M. A. 2014, *ApJL*, 790, L35
- Bromm, V., & Loeb, A. 2003, *Nature*, 425, 812
- Caffau, E., Bonifacio, P., François, P., et al. 2011, *Nature*, 477, 67
- Carilli, C. L. 2011, *ApJL*, 730, L30
- Carollo, D., Freeman, K., Beers, T. C., et al. 2014, *ApJ*, 788, 180
- Cazaux, S., & Spaans, M. 2004, *ApJ*, 611, 40
- Cazaux, S., & Tielens, A. G. G. M. 2002, *ApJ*, 575, L29
- Chen, P., Wise, J. H., Norman, M. L., Xu, H., & O’Shea, B. W. 2014, eprint arXiv:1408.2523
- Chiaki, G., Nozawa, T., & Yoshida, N. 2013, *ApJ*, 765, L3
- Cuppen, H. M., Ioppolo, S., Romanzin, C., & Linnartz, H. 2010, *Physical Chemistry Chemical Physics (Incorporating Faraday Transactions)*, 12, 12077
- Dalgarno, A. 2006, *PNAS*, 103, 12269
- Dalgarno, A., & Black, J. H. 1976, *Reports on Progress in Physics*, 39, 573
- Dalgarno, A., & McCray, R. A. 1973, *ApJ*, 181, 95
- de Jong, T. 1972, *AA*, 20, 263
- de Nijs, A. J., Ubachs, W., & Bethlem, H. L. 2012, *PRA*, 86, 032501
- Dopcke, G., Glover, S. C. O., Clark, P. C., & Klessen, R. S. 2011, *ApJ*, 729, L3
- Draine, B. T. 1978, *ApJS*, 36, 595
- . 2003, *ApJ*, 598, 1017
- . 2011, *Physics of the Interstellar and Intergalactic Medium* (Princeton, NJ: Princeton Univ. Press)
- Förster Schreiber, N. M., Genzel, R., Bouché, N., et al. 2009, *ApJ*, 706, 1364
- Frebel, A., Simon, J. D., & Kirby, E. N. 2014, *ApJ*, 786, 74
- Glover, S. C. O. 2003, *ApJ*, 584, 331
- Glover, S. C. O., & Clark, P. C. 2014, *MNRAS*, 437, 9
- Glover, S. C. O., & Jappsen, A.-K. 2007, *ApJ*, 666, 1
- Graedel, T. E., Langer, W. D., & Frerking, M. A. 1982, *ApJS*, 48, 321
- Grebe, J., & Homann, K. H. 1982, *Berichte der Bunsengesellschaft für Phys. Chemie*, 86, 587
- Gredel, R., Lepp, S., Dalgarno, A., & Herbst, E. 1989, *ApJ*, 347, 289
- Hailey-Dunsheath, S., Sturm, E., Fischer, J., et al. 2012, *ApJ*, 755, 57
- Harding, L. B., Guadagnini, R., & Schatz, G. C. 1993, *J. Phys. Chem.*, 97, 5472
- Harwit, M., & Spaans, M. 2003, *ApJ*, 589, 53
- Heays, A. N., Visser, R., Gredel, R., et al. 2014, *AA*, 562, A61
- Herbst, E., & Klemperer, W. 1973, *ApJ*, 185, 505
- Heywood, I., Armstrong, R. P., Booth, R., et al. 2011, eprint arXiv:1103.0862
- Hinshaw, G., Larson, D., Komatsu, E., et al. 2013, *ApJS*, 208, 19
- Hollenbach, D., Kaufman, M. J., Bergin, E. A., & Melnick, G. J. 2009, *ApJ*, 690, 1497
- Hollenbach, D., Kaufman, M. J., Neufeld, D., Wolfire, M., & Goicoechea, J. R. 2012, *ApJ*, 754, 105
- Hollenbach, D., & McKee, C. F. 1989, *ApJ*, 342, 306
- Hollenbach, D. J., Werner, M. W., & Salpeter, E. E. 1971, *ApJ*, 163, 165
- Igea, J., & Glassgold, A. E. 1999, *ApJ*, 518, 848
- Indriolo, N., & McCall, B. J. 2012, *ApJ*, 745, 91
- Jappsen, A.-K., Klessen, R. S., Glover, S. C. O., & Mac Low, M.-M. 2009a, *ApJ*, 696, 1065
- Jappsen, A.-K., Mac Low, M.-M., Glover, S. C. O., Klessen, R. S., & Kitsionas, S. 2009b, *ApJ*, 694, 1161
- Jura, M. 1974, *ApJ*, 191, 375
- Kanekar, N., Chengalur, J. N., & Ghosh, T. 2004, *Physical Review Letters*, 93, 051302
- Kanekar, N., Langston, G. I., Stocke, J. T., Carilli, C. L., & Menten, K. M. 2012, *ApJL*, 746, L16
- Klessen, R. S., Glover, S. C. O., & Clark, P. C. 2012, *MNRAS*, 421, 3217
- Kozlov, M. G., & Levshakov, S. A. 2013, *Annalen der Physik*, 525, 452
- Lamberts, T., Cuppen, H. M., Fedoseev, G., et al. 2014, *AA*, 570, A57
- Latif, M. A., Bovino, S., Grassi, T., Schleicher, D. R. G., & Spaans, M. 2015, *MNRAS*, 446, 3163
- Le Bourlot, J., Pineau des Forets, G., Roueff, E., & Schilke, P. 1993, *ApJ*, 416, L87
- Le Teuff, Y. H., Millar, T. J., & Markwick, A. J. 2000, *AAS*, 146, 157
- Lee, H.-H., Roueff, E., Pineau des Forets, G., et al. 1998, *AA*, 334, 1047
- Lepp, S., & Dalgarno, A. 1996, *AA*, 306, L21
- Lepp, S., & Tiné, S. 1998, in *The Molecular Astrophysics of Stars and Galaxies*, ed., T.W. Hartquist and D.A. Williams. Clarendon Press, Oxford, p. 489.
- Lidz, A., Furlanetto, S. R., Oh, S. P., et al. 2011, *ApJ*, 741, 70
- Maloney, P. R., Hollenbach, D. J., & Tielens, A. G. G. M. 1996, *ApJ*, 466, 561
- Mannucci, F., Cresci, G., Maiolino, R., Marconi, A., & Gnerucci, A. 2010, *MNRAS*, 408, 2115
- Mashian, N., Sternberg, A., & Loeb, A. 2013, *MNRAS*, 435, 2407
- McCall, B. J., Huneycutt, A. J., Saykally, R. J., et al. 2003, *Nature*, 422, 500
- McElroy, D., Walsh, C., Markwick, A. J., et al. 2013, *AA*, 550, A36
- McKee, C. F., & Ostriker, E. C. 2007, *ARAA*, 45, 565
- Meijerink, R., & Spaans, M. 2005, *AA*, 436, 397
- Miyake, S., Stancil, P. C., Sadeghpour, H. R., et al. 2010, *ApJ*, 709, L168
- Muñoz, J. A., & Furlanetto, S. R. 2013, *MNRAS*, 435, 2676
- Neufeld, D. A., & Dalgarno, A. 1989, *ApJ*, 340, 869
- Neufeld, D. A., Goicoechea, J. R., Sonnentrucker, P., et al. 2010, *AA*, 521, L10
- Norris, J. E., Yong, D., Bessell, M. S., et al. 2013, *ApJ*, 762, 28
- Omukai, K. 2000, *ApJ*, 534, 809
- Omukai, K. 2012, *PASJ*, 64, 114
- Omukai, K., Hosokawa, T., & Yoshida, N. 2010, *ApJ*, 722, 1793
- Omukai, K., Tsuribe, T., Schneider, R., & Ferrara, A. 2005, *ApJ*, 626, 627
- Oppenheimer, M., & Dalgarno, A. 1974, *ApJ*, 192, 29
- Papadopoulos, P. P. 2010, *ApJ*, 720, 226
- Penprase, B. E., Prochaska, J. X., Sargent, W. L. W., Toro-Martinez, I., & Beeler, D. J. 2010, *ApJ*, 721, 1
- Penteado, E. M., Cuppen, H. M., & Rocha-Pinto, H. J. 2014, *MNRAS*, 439, 3616
- Pettini, M., Zych, B. J., Steidel, C. C., & Chaffee, F. H. 2008, *MNRAS*, 385, 2011
- Pineau des Forets, G., Roueff, E., & Flower, D. R. 1992, *MNRAS*, 258, 45P
- Rafelski, M., Wolfe, A. M., Prochaska, J. X., Neeleman, M., &

- Mendez, A. J. 2012, *ApJ*, 755, 89
- Safraneck-Shrader, C., Milosavljević, M., & Bromm, V. 2014, *MNRAS*, 438, 1669
- Santoro, F., & Shull, J. M. 2006, *ApJ*, 643, 26
- Schneider, R., Ferrara, A., Natarajan, P., & Omukai, K. 2002, *ApJ*, 571, 30
- Schneider, R., Omukai, K., Inoue, A. K., & Ferrara, A. 2006, *MNRAS*, 369, 1437
- Stäuber, P., Doty, S. D., van Dishoeck, E. F., & Benz, A. O. 2005, *AA*, 440, 949
- Sternberg, A., & Dalgarno, A. 1995, *ApJS*, 99, 565
- Sternberg, A., Dalgarno, A., & Lepp, S. 1987, *ApJ*, 320, 676
- Sternberg, A., Dalgarno, A., Pei, Y., & Herbst, E. 2011, *EAS Publ. Ser.*, 52, 43
- Sternberg, A., Le Petit, F., Roueff, E., & Le Bourlot, J. 2014, *ApJ*, 790, 10
- Tacconi, L. J., Neri, R., Genzel, R., et al. 2013, *ApJ*, 768, 74
- Tafelmeyer, M., Jablonka, P., Hill, V., et al. 2010, *AA*, 524, A58
- Tielens, A. G. G. M. 2013, *Rev. Mod. Phys.*, 85, 1021
- Tremonti, C. A., Heckman, T. M., Kauffmann, G., et al. 2004, *ApJ*, 613, 898
- Truppe, S., Hendricks, R. J., Tokunaga, S. K., et al. 2013, *Nature Communications*, 4, 2600
- van der Tak, F. F. S., & van Dishoeck, E. F. 2000, *AA*, 358, L79
- van Dishoeck, E. F. 1988, in *Millimetre and Submillimetre Astronomy*, ed. R.D Wolstencroft and W.B. Burton, Kluwer, Dordrecht, p.117
- . 1998, in *The Molecular Astrophysics of Stars and galaxies*, ed. T.W. Hartquist and D.A. Williams, Clarendon Press, Oxford, p.53
- van Dishoeck, E. F., & Black, J. H. 1986, *ApJS*, 62, 109
- van Dishoeck, E. F., Herbst, E., & Neufeld, D. A. 2013, *Chem. Rev.*, 113, 9043
- van Dishoeck, E. F., Jonkheid, B., & van Hemert, M. C. 2006, *Faraday Discuss.*, 133, 231
- Vasyunin, A. I., Semenov, D., Henning, T., et al. 2008, *ApJ*, 672, 629
- Vejby-Christensen, L., Andersen, L. H., Heber, O., et al. 1997, *ApJ*, 483, 531
- Visser, R., van Dishoeck, E. F., & Black, J. H. 2009, *AA*, 503, 323
- Volonteri, M., & Silk, J. 2014, eprint arXiv:1401.3513
- Vonlanthen, P., Rauscher, T., Winteler, C., et al. 2009, *AA*, 503, 47
- Wakelam, V., Herbst, E., Selsis, F., & Massacrier, G. 2006, *AA*, 459, 813
- Wakelam, V., Herbst, E., Loison, J.-C., et al. 2012, *ApJS*, 199, 21
- Walsh, C., Harada, N., Herbst, E., & Millar, T. J. 2009, *ApJ*, 700, 752
- Whitaker, K. E., van Dokkum, P. G., Brammer, G., & Franx, M. 2012, *ApJ*, 754, L29
- Yan, M. 1997, Thesis, Harvard Univ.
- Yong, D., Norris, J. E., Bessell, M. S., et al. 2013, *ApJ*, 762, 27